PIAG_GA_2011-286397-R6

Date: 2016-01-31

Report

Enhanced permafrost creep model– user manual and documentation

For

by:
Seyed Ali Ghoreishian Amiri
Mehdi Kadivar

(sign.)

Project manager:
Gustav Grimstad

(sign.)

Creep of Geomaterials

Summary

The mechanical behavior of frozen soils is one of the challenging topics in the field of geotechnical engineering. The behavior of frozen soils is strongly affected by the amount of ice, while on the other hand, the amount of ice depends on the temperature and the applied mechanical stresses. The influence of ice content and temperature on the mechanical behavior and the coupling effects on the reverse direction can be mentioned as the main difference between the behavior of frozen and unfrozen soils. In the light of this difference, an elastoplastic constitutive model for describing the stress-strain behavior of saturated frozen soils is proposed. By dividing the total stress into fluid pressure and solid phase stress, in addition to consideration of the cryogenic suction, the model is formulated within the framework of two-stress state variables. The proposed model is able to represent many of fundamental features of the behavior of frozen soils such as ice segregation phenomenon and strength weakening due to pressure melting. In unfrozen state the model becomes a conventional critical state model.

On the other hand, considering the highly rate dependent behavior of ice, highly rate sensitive behavior of frozen soil is expected. Thus, creep deformation of frozen soils, specifically in permafrost, is of great importance. So, the above mentioned elastic-plastic model is developed to an elastic-viscoplastic model to be able to simulate the rate effect and its consequent creep deformation.

Typical predictions of the model for simulating the characteristic trends of the frozen soil behavior is described qualitatively. Model predictions are also compared with the available test results and reasonable agreement is achieved.

Content

1 Introduction

Permafrost is defined as ground that remains at or below 0°C for at least two consecutive years. It is geographically widespread, occupying approximately 24 percent of the exposed land surface in the Northern Hemisphere [1]. Figure 1.1 shows the distribution of permafrost in the Northern Hemisphere.

Since the previous decades, the need for energy sources, raw materials, and constructed facilities is growing rapidly, and the interest in regions with frozen ground has highly increased. With the increase in construction of infrastructures, such as highways, pipelines, tunnels, and railways, in cold regions, it is essential to stablish a reasonable constitute model for frozen soils.

So far, many research activities have been conducted on mechanical behavior of frozen soils and a significant amount of valuable information have been presented. However, there are still many uncertainties and model shortcomings in this field and still a lot of research has to be done. Engineering designs in these regions required a deep understanding of the behavior of frozen soils as well as the ability of simulation. Simulating engineering problems required an appropriate constitutive model, which is able to represent the fundamental features of the mechanical behavior.

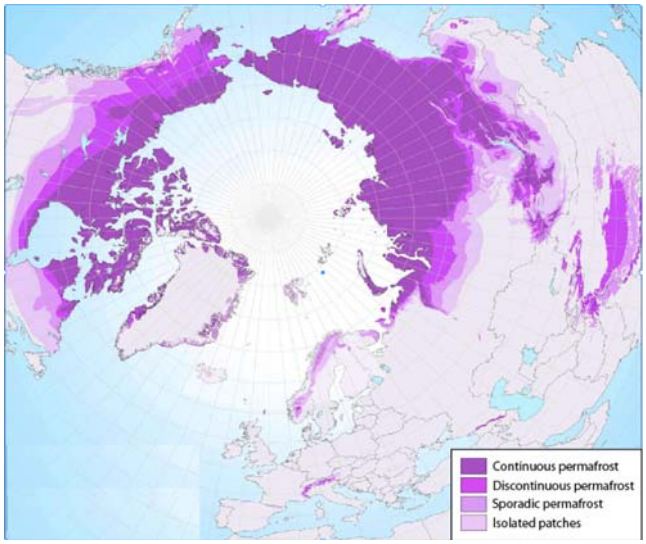

Figure 1.1 : Distribution of permafrost in Northern Hemisphere. (Source: International Permafrost Association)

1.1 State of the art

The constitutive modeling of frozen soils has been closely linked with identifying the relevant stress measurements describing the stress-strain behavior. Total stress-based models have been widely used in the literature to describe the mechanical behavior of frozen soils [2-10]. However, it seems that they only tended to accentuate the influence of confining pressure on the elastic-plastic behavior, placing less emphasis on the influence of other very important factors such as temperature and ice content. In other words, these models cannot simulate deformations under the variation of ice content and/or temperature during a freezing or thawing period. Moreover, working with total stress, description of

soil behavior in the presence of unfrozen water will face some significant difficulties which are not clearly addressed in the models.

The effective stress principle by means of total stress minus pore pressure is employed by some researchers to simulate the behavior of frozen soils [11-14]. However, different definitions of pore pressure are used in different models. Nicolsky et al. [12] and Li et al. [13] used a combination of unfrozen water pressure and ice pressure, but Nixon [11] and Thomas et al. [14] preferred to have a switch between water and ice pressure in partially frozen and fully frozen states. This approach is pragmatically appropriate for simulating ice segregation phenomenon during a freezing period. However, soil strength after ice segregation is the main problem of this approach.

Nishimura et al. [15] are the first to propose a two-stress state variables model for simulating the behavior of frozen soils by employing the net stress (as the excess of total stress over ice pressure) and the cryogenic suction as the relevant stress variables. In this model, increase of ice pressure, during a freezing period, results in zero or negative values of net mean stress, and is followed by a tensile failure and soil particles segregation. This results in an increase in void ratio and a softer behavior of the soil. In unfrozen state, the model reduces to an effective stress-based critical state model by replacing water pressure instead of ice pressure in the definition of net stress. Hence, simulating of thawing consolidation is also possible by switching to the effective stress principle. The issue is that, samples which has experienced a tensile failure (due to segregation phenomenon) by decreasing temperature under isotropic stress condition, will always show dilative behavior upon shearing.

Zhou [16] proposed another approach in the framework of two-stress state variables by considering the temperature during freezing as the second independent variable, instead of suction. Moreover, in this model, the dependency of failure criterion on temperature and ice content of frozen soil obtained through a strength upscaling procedure based on the microstructures of the mixture. Considering the identity of stress measurement and yield mechanism for ice segregation phenomenon between this model and that introduced by Nishimura et al. [15], the previously mentioned problem for shearing a sample after freezing under isotropic stress condition is still remained.

Zhang and Michalowski [17] employed the effective stress (i.e. total stress minus water pressure) and the pore ice ratio (i.e. the ratio of the volume of ice on the volume of solid particles) as the independent variables for their constitutive model. However, this kind of effective stress would create an unrealistically high effective confining pressure, if the unfrozen water content approaches zero. The frost heave phenomenon, in this model, is simulated using a porosity growth function.

1.2 Objective and scope

In this research, main features of the behavior of frozen soils are reviewed and explained by considering the physic of the system. The analogy and difference of cryogenic suction in freezing soils and matric suction in unsaturated soils are explored. The concept of the framework, which is consistent with the physic of the process, is then described in details. The model is verified with some laboratory

tests in one integration point simulations. The proposed model is then implemented to PLAXIS and used to solve a boundary value problem.

1.3 Structure

In addition to this introduction, the report is arranged in 4 chapters as indicated below:

Chapter 2 presents the main features of behavior of saturated frozen soil by reviewing the effects of temperature, ice content, confining pressure and strain rate. It also describes the concept of cryogenic suction and explores the analogy and difference of cryogenic suction in freezing soils and matric suction in unsaturated soils. Appropriate stress measurement for simulating the fundamental features of the behavior is also illustrated in this chapter.

Chapter 3 introduces the elastic-plastic model for simulating the rate-independent behavior of frozen soils. It ends with verification of the model with available test results and qualitatively description of typical predictions of the model for simulating the characteristic trends of the frozen soil behavior.

Chapter 4 extends the elastic-plastic formulation to the elastic-viscoplastic case. The extended model is able to simulate the rate dependent behavior and creep deformations. The model is verified with available test results.

Chapter 5 uses the implemented elastic-viscoplastic model to solve a realistic boundary value problem. The user manual is also included in this chapter.

2 Features of the behavior and main concepts

From the point of view of material science, saturated frozen soil is a natural particulate composite, composed of solid grains, ice and unfrozen water. In frozen soils, due to existence of ice and its interaction with solid grains and unfrozen water, temperature and ice content are the additional factors influencing the behavior.

2.1 Major factors

2.1.1 Ice content

Experimental results show that at lower ice content, strength of the mixture rises with increasing ice content, but after a certain value of ice content, strength will decrease with increasing ice content [18, 19]. Actually, in poor ice soils, when the volume of ice is less than t pores volume, presence of ice in soil pores causes the grains to bind together. While, in ice rich soils, the porosity is almost filled by ice, thus, an increase in ice content results in a decrease in soil contacts by segregating the particles. This behavior is shown in figure 2.1.

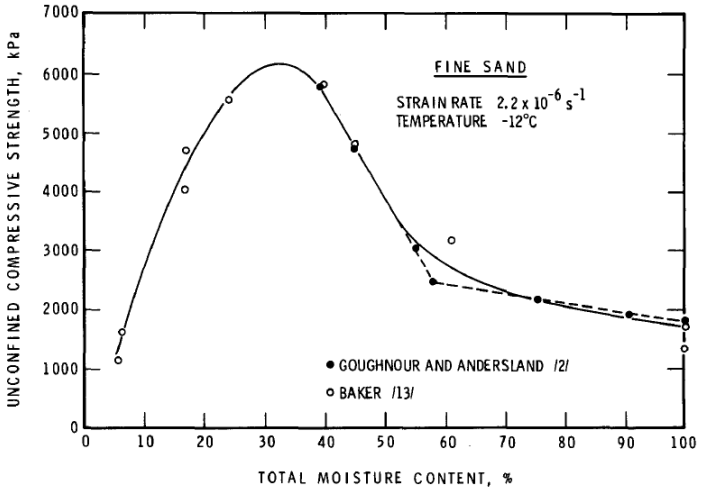

Figure 2.1 Effect of the total moisture content on unconfined compressive strength of a frozen sand at constant temperature and strain rate (After Baker [18])

2.1.2 Temperature

Many test results show that the temperature is the most important parameter which controls the mechanical properties of frozen soils [20-23]. The temperature strongly effects the mechanical properties of ice and the bonding strength of the interface between soil particles and ice.

Xie et al. [24] showed the influence of temperature on the stress-strain curves (figure 2.2). As shown in the figure, the slope of the first stage of the curves increases with decreasing temperature. Actually, if the temperature decreases, the amount of ice in the sample will increases and so, more brittle behavior can be observed. Similar behavior is also reported in [6, 25].

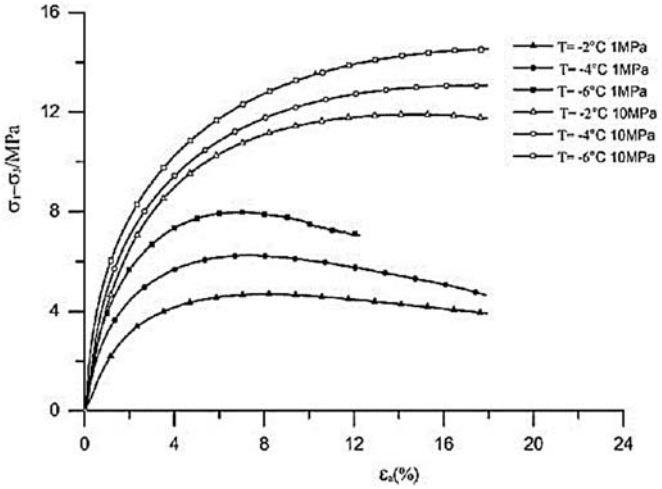

Figure 2.2 Stress-strain curves of frozen soil at different confining pressures and temperatures (After Yuanming et al. [6])

2.1.3 Confining pressure

The behavior of frozen soils under the variation of confining pressure are reported by many researchers [21, 26-29]. It is found, at lower confining pressure, the strength of frozen soil will increase by increasing confining pressure, while after a threshold value, strength reduction by increasing confining pressure is reported. Further increasing of the confining pressure causes another change in the direction of the behavior, and strength will start to increase again by confining pressure. This behavior is shown in figure 2.3 in three different regions:

1. The low stress region I: the triaxial behavior is 'normal'; strength increases with the confining pressure.
2. The mid-pressure region II: In this region, shear strength decreases with increasing mean stress.
3. The high pressure region III: In the third region, the strength increases with mean stress.

The behavior of frozen soils under the variation of confining pressure can be considered to be the result of combined mechanical and thermodynamic effects, the former governs the stress sharing, while the latter the pressure melting phenomenon.

2.1.4 Strain rate

Considering the highly rate dependent behavior of ice, highly rate sensitive behavior of frozen soil is expected. The influence of strain rate on the mechanical behavior of frozen soils is shown in figure 2.4. As shown in the figure, the mobilized deviatoric stresses grow in the beginning very rapidly. This happens because of the stiffening effect of the pore ice. After reaching a maximum value, the stress drops to a lower value as the bonds between soil grains and ice are cracking [27]. Similar behavior is also reported in [24, 25].

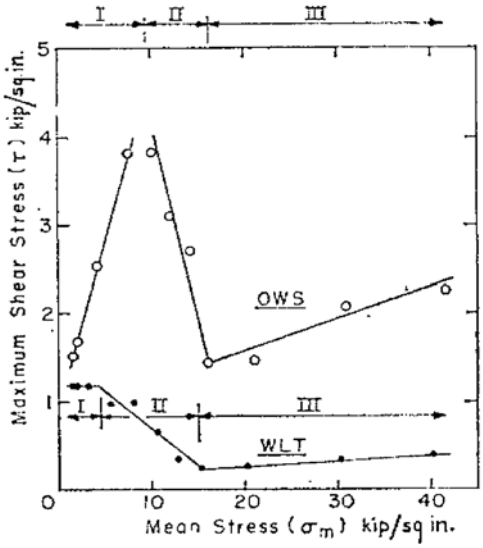

Figure 2.3 Variation of strength with confining pressure (After Chamberlain et al. [26])

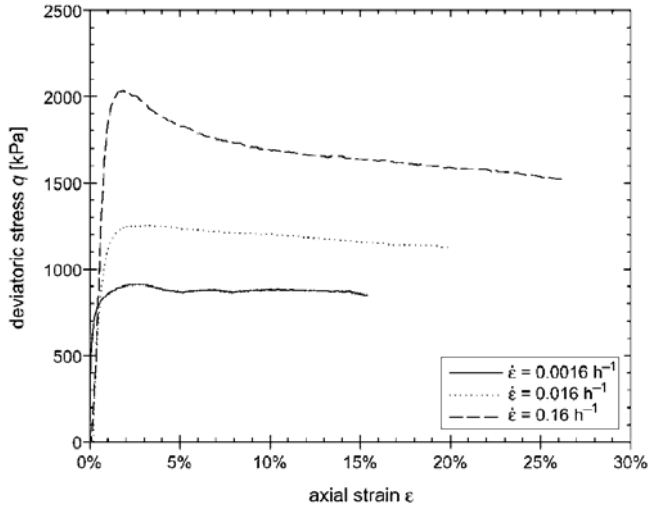

Figure 2.4 Stress-strain curves of frozen soil at different strain rates

2.2 Conceptual model

Considering the Clausius-Clapeyron equation as the requirement of equilibrium between ice and liquid water phases [30], the cryogenic suction can be calculated by [14]

$$S = p_i - p_w = -\rho_i l \ln \frac{T}{T_0} \tag{2.1}$$

where S is the cryogenic suction, p_w and p_i denote the pressure of water and ice phases, respectively, ρ_i indicates the density of ice, l is the specific latent heat of fusion, T stands for temperature on the thermodynamic scale and T_0 is the freezing/thawing temperature of water/ice at the given pressure. Equation (2.1) indicates that the variation of temperature can be captured by the variation of cryogenic suction.

On the other hand, according to Tice et al. [31], ice content can be represented as a function of temperature and consequently as a function of cryogenic suction. Many researchers proposed different freezing characteristic functions to explain this dependency [e.g. [15, 32-36]]. Hence, the variation of ice content can also be represented by the variation of cryogenic suction.

According to above description, studying the effect of cryogenic suction is essential to understand the behavior of frozen soils. Wettlaufer and Worster [37] showed, there exists two types of mechanisms that allow water to remain in unfrozen state at temperature below the bulk freezing point: curvature-induced premelting and interfacial premelting (figure 2.5). The former is the result of surface tension and acts very similar to the capillary suction by bonding the grains together. Whereas the latter is the result of disjoining pressure (as a repelling force between ice and solid grains) and tends to widen the gap by sucking in more water [16, 37-39]. The combination of these mechanisms controls the behavior regarding the ice content and temperature variations.

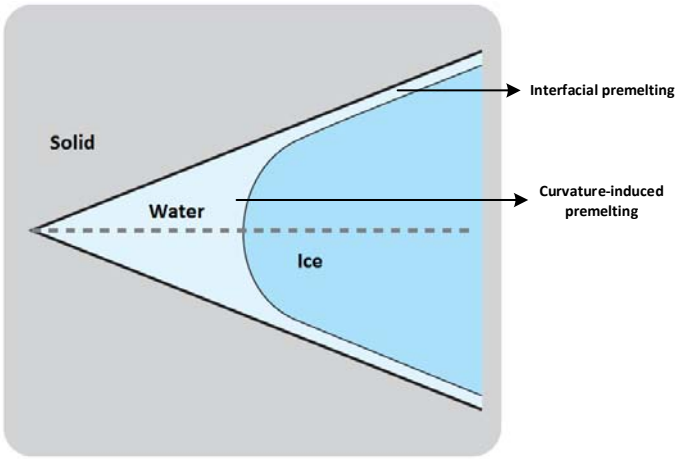

Figure 2.5 Curvature induced premelting and interfacial premelting during intrusion of ice into a wedge-shape wet preferential solid (After Zhou [16])

The premelting theory can describe the behavior of frozen soils at different ice content (as discussed in section 2.1.1). At lower ice content, the behavior is dominated by the curvature-induced premelting mechanism which results in higher strength of the soil, while at higher ice content, the behavior is dominated by the interfacial premelting mechanism and followed by strength weakening of the soil due to grains segregation. Note that since the interfacial premelting mechanism acts by sucking in

more water, availability of water is essential to have a higher influence of the interfacial premelting mechanism.

The effect of temperature variation on the behavior of frozen soil (regardless of its indirect effect through the variation of ice content; section 2.1.2), can be easily simulated by defining the elastic parameters of the system as a function of temperature.

As discussed in section 2.1.3, the behavior of frozen soils under the variation of confining pressure is considered to be the result of the stress sharing and the pressure melting phenomenon. For simulating this behavior, a pressure dependent freezing/thawing temperature of ice (T_0 in equation 2.1) is required. Thus, due to pressure melting, the freezing/thawing temperature will decrease and results in an increase in water pressure and a decrease in cryogenic suction. So, the strength weakening can be considered as the result of increasing water pressure and decreasing cryogenic suction. This behavior can be captured by using a kind of effective stress and a suction-dependent yield criterion. The former reflects the effect of water pressure, while the later the effect of cryogenic suction.

For simulating the effect of strain rate (section 2.1.4), the isotach concept [40] can be considered. Suklje [40] postulated that, there is a unique relationship between the void ratio, effective stress and rate of deformation. He shows, the relationship stays unique during primary and secondary consolidation. The isotach model was then followed by many other researchers (e.g. [41-43]) to simulate the creep deformation of soils.

2.3 Stress measurement

Considering ice crystals as a part of the solid phase, a saturated frozen soil can be viewed as a porous material in which the pores are filled with water. Hence, a kind of effective stress, which can be called the *solid phase stress*, is defined

$$\boldsymbol{\sigma}^* = \boldsymbol{\sigma} - s_w p_w \boldsymbol{I} \qquad (2.2)$$

where $\boldsymbol{\sigma}^*$ is the solid phase stress, s_w is the unfrozen water saturation (i.e. the ratio of the volume of unfrozen water on the volume of frozen and unfrozen water), and $\boldsymbol{I}$ denotes a unit tensor. The solid phase stress is actually considered as the combined stress of soil grains and ice. In equation (2.2), unfrozen water saturation is involved due to the fact that the effect of water pressure on the stress state of the solid phase is dependent on the contact area of the phases. For instance, at very low unfrozen water saturation , water pressure cannot affect the state of stress in the solid phase.

The solid phase stress can reflect the effect of unfrozen water. While, the effects of ice content and temperature variation can be taken into account by considering the cryogenic suction as the second stress state variable. A suction-dependent yield criteria can capture the effect of the curvature-induced premelting mechanism by expanding the yield surface with suction. Variation of suction with respect to the curvature-induced premelting mechanism, which acts by bonding the grains together, results in compressive deformation of the soil. In the proposed model, this deformation is considered as the elastic part of deformation due to suction variation. On the other hand, domination of the behavior by

the interfacial premelting mechanism can be reflected in the model by defining another yield criterion for grain segregation due to more increase of suction. Variation of suction with respect to the interfacial premelting mechanism, which acts as a kind of thermodynamic buoyancy, results in expansion of the soil. This is the major part of deformation and will appear when the film of unfrozen water becomes enough thin (figure 2.5). In the proposed model, this deformation is considered as the irrecoverable part of deformation due to suction variation.

3 Elastic-plastic model

3.1 Strain decomposition

Following the discussion in section 2.3, any strain increment, $d\boldsymbol{\varepsilon}$, can be additively decomposed into the following parts

$$d\boldsymbol{\varepsilon} = d\boldsymbol{\varepsilon}^{me} + d\boldsymbol{\varepsilon}^{se} + d\boldsymbol{\varepsilon}^{mp} + d\boldsymbol{\varepsilon}^{sp} \tag{3.1}$$

where $d\boldsymbol{\varepsilon}^{me}$ and $d\boldsymbol{\varepsilon}^{mp}$ are the elastic and plastic parts of strain due to the solid phase stress variation, $d\boldsymbol{\varepsilon}^{se}$ and $d\boldsymbol{\varepsilon}^{sp}$ are the elastic and plastic parts of strain due to the cryogenic suction variation, respectively.

Note that throughout the formulation, compressive stress and strain are assumed to be positive.

3.2 Model formulation

3.2.1 Elastic response

The elastic part of strain due to the solid phase stress variation can be calculated based on the equivalent elastic parameters of the mixture

$$G = (1 - s_i)G_0 + \frac{s_i E_f}{2(1+\nu_f)} \tag{3.2}$$

$$K = (1 - s_i)\frac{(1+e)p^*_{y_0}}{\kappa_0} + \frac{s_i E_f}{3(1-2\nu_f)} \tag{3.3}$$

where G and K are the equivalent shear modulus and bulk modulus of the mixture, respectively, G_0 and κ_0 stand for the shear modulus and the elastic compressibility coefficient of the soil in an unfrozen state, respectively, $p^*_{y_0}$ is the preconsolidation stress for unfrozen condition, E_f and ν_f denote the Young's modulus and Poisson's ratio of the soil in the fully frozen state, respectively, and s_i is the ice saturation. Considering the temperature-dependent behavior of ice, the following expression is employed for E_f

$$E_f = E_{f_{ref}} - E_{f_{inc}}\left(T - T_{ref}\right) \tag{3.4}$$

where $E_{f_{ref}}$ is the value of E_i at the reference temperature (T_{ref}) and $E_{f_{inc}}$ denotes the rate of change in E_f with temperature.

The elastic part of strain due to suction variation is calculated as

$$d\boldsymbol{\varepsilon}^{se} = \frac{\kappa_s}{3(1+e)} \times \frac{dS}{(S+p_{at})} \boldsymbol{I} \tag{3.5}$$

where κ_s is the compressibility coefficient due to suction variation within the elastic region, e is the void ratio and p_{at} is the atmospheric pressure.

3.2.2 Yield surfaces

For consistency, when the value of cryogenic suction becomes zero, the model should reduce to a common unfrozen soil model. In accordance with the aim of simplicity, the simple modified Cam-clay model is adopted for unfrozen state. However, the framework presented here could be coupled to more complex models, achieving a better representation of some aspects of soil behavior such as strength anisotropy or destructuration.

For frozen state, a suction-dependent yield function is needed to capture the curvature-induced premelting effects. Due to lack of experimental data, this dependency is borrowed from unsaturated soil models. Hence, based on the Barcelona Basic Model (BBM) [44] the yield surface due to variation of solid phase stress is expressed as

$$F_1 = \left[p^* - \left(\frac{p_y^* - k_t S}{2} \right) \right]^2 + \left(\frac{q^*}{M} \right)^2 - \left(\frac{p_y^* + k_t S}{2} \right)^2 = 0. \tag{3.6}$$

where

$$p_y^* = p_c^* \left(\frac{p_{y_0}^*}{p_c^*} \right)^{\frac{\lambda_0 - \kappa}{\lambda - \kappa}} \tag{3.7}$$

$$\lambda = \lambda_0 \left[(1-r)\exp(-\beta S) + \mathrm{r} \right] \tag{3.8}$$

and p^* is the solid phase mean stress, q^* denotes the solid phase deviatoric stress, M stands for the slope of the critical state line, k_t is the parameter for describing the increase in apparent cohesion with suction, p_c^* indicates the reference stress, κ denotes the compressibility coefficient of the system within the elastic region ($\kappa = \frac{1+e}{K} p_{y_0}^*$), λ_0 represents the compressibility coefficient for the unfrozen state along virgin loading, r is a constant related to the maximum stiffness of the soil (for infinite cryogenic suction) and β is a parameter controlling the rate of change in soil stiffness with suction. Based on the BBM, this yield surface is recognized as the Loading Collapse (LC) yield surface.

As reviewed in the previous section, increase of cryogenic suction will lead to grain segregation (commonly recognized as ice segregation phenomenon) when the behavior is dominated by the interfacial premelting mechanism. The Grain Segregation (GS) yield criterion is adopted as

$$F_2 = S - S_{seg} = 0. \tag{3.9}$$

where S_{seg} is the threshold value of suction for ice segregation phenomenon. Figure 3.1 shows the complete yield surfaces of the model in $p^* - q^* - S$ space.

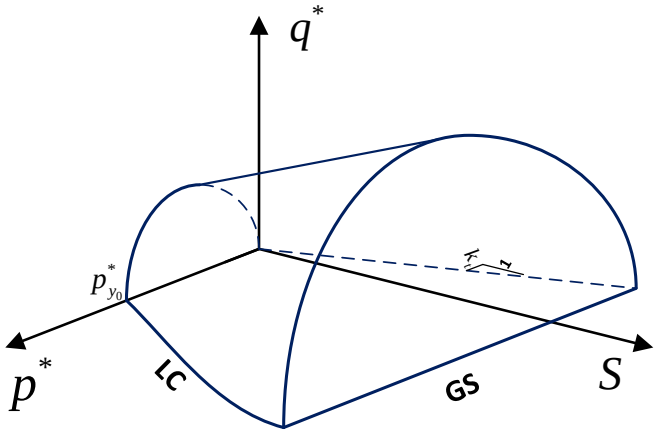

Figure 3.1 Three-dimensional view of the yield surfaces in p^* - q^* - S space

3.2.3 Hardening rules

A plastic compression due to the variation of solid phase stress results in stiffer behavior of the soil and causes the LC yield surface to move outward. Furthermore, this plastic compression results in a decrease in the dimensions of voids, hence, lower segregation threshold value is expected. This behavior could be captured by a coupled hardening rule, which causes the GS yield surface to shift downward. Figure 3.2 shows a typical evolution of yield surfaces due to a plastic compression in $p^* - S$ and $p^* - q^*$ planes.

A plastic dilation due to occurrence of ice segregation causes the GS yield surface to move upward. This plastic dilation results in softer behavior of the soil, hence, an inward movement of the LC yield surface should also be considered (figure 3.3).

Adapting a linear dependence between specific volume (v) and $\ln p^*$, both in the elastic-plastic and elastic range, the plastic component of volumetric strain due to an increase in p^* along the virgin state, can be computed as:

$$d\varepsilon_v^{mp} = \frac{\lambda - \kappa}{1+e}\frac{dp_y^*}{p_y^*} \tag{3.10}$$

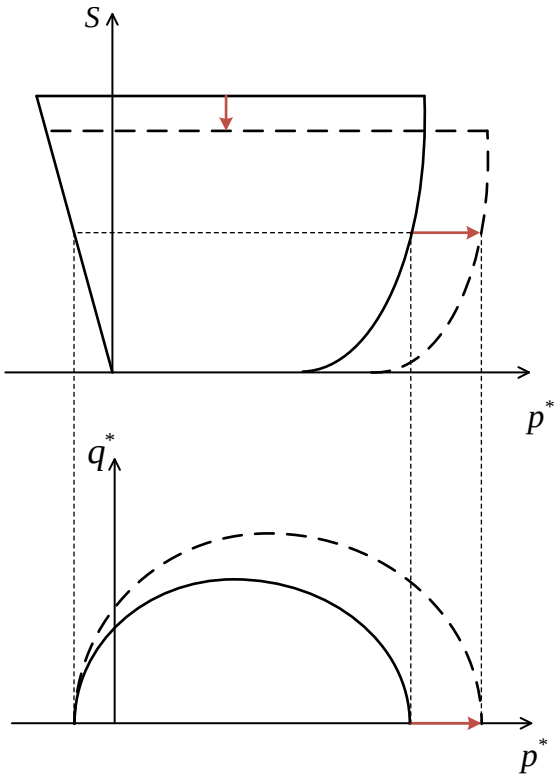

Figure 3.2 Evolution of yield surfaces due to plastic compression

Taking into account equation (3.7), it is simple to show that the plastic volumetric strain (3.10) is also given by

$$d\varepsilon_v^{mp} = \frac{\lambda_0 - \kappa_0}{1+e}\frac{dp_{y_0}^*}{p_{y_0}^*} \tag{3.11}$$

Rearranging equation (3.11), one can write:

$$\frac{dp_{y_0}^*}{p_{y_0}^*} = \frac{1+e}{\lambda_0 - \kappa_0} d\varepsilon_v^{mp} \tag{3.12}$$

Assuming similar effect from the plastic deformation due to suction variation, the hardening rule for LC yield surface is proposed as follows

$$\frac{dp_{y_0}^*}{p_{y_0}^*} = \frac{1+e}{\lambda_0 - \kappa_0} d\varepsilon_v^{mp} + \frac{1+e}{\lambda_0 - \kappa_0} d\varepsilon_v^{sp} \tag{3.13}$$

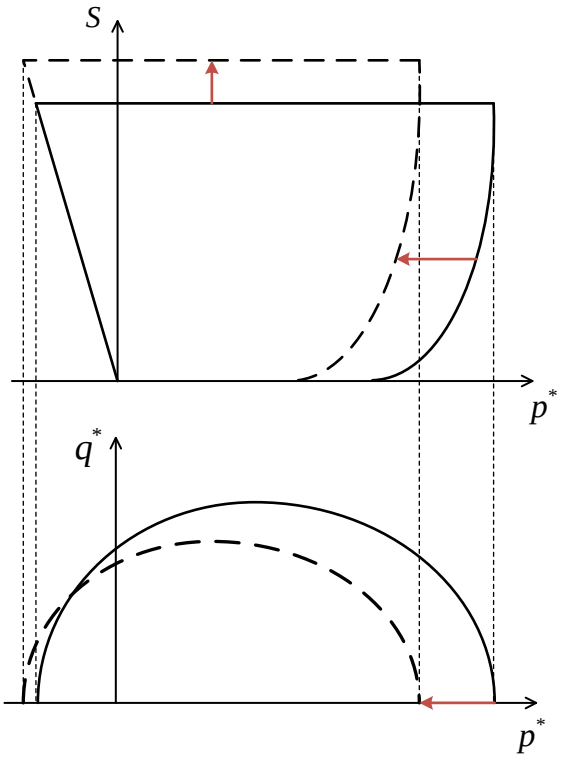

Figure 3.3 Evolution of yield surfaces due to ice segregation phenomenon

Adopting the same assumptions for the behavior in $v:\ln(S+p_{at})$ plane, and considering the contractile and dilative behavior of the soil with respect to the curvature-induced and interfacial premelting mechanisms, the evolution of the GS yield surface can be considered as

$$\frac{dS_{seg}}{S_{seg}+p_{at}}=-\frac{1+e}{(\lambda_s+\kappa_s)}d\varepsilon_v^{sp}-\frac{1+e}{(\lambda_s+\kappa_s)}d\varepsilon_v^{mp} \tag{3.14}$$

However, as mentioned in the previous chapter, the amount of strain due to interfacial premelting mechanism depends on the availability of water. The lower unfrozen water saturation of the freezing fringe, the lower permeability for water to be sucked in. This results in a smaller amount of strain due to increase of cryogenic suction. In other words, plastic resistance of the soil, which is the result of the hardening rule, increases by decreasing water saturation. In addition, by increasing ice content, effect of plastic deformation due to mechanical loading, on the segregation threshold value becomes lower and lower. Adopting these modifications, the hardening rule of the GS yield surface is proposed as follows

$$\frac{dS_{seg}}{S_{seg}+p_{at}}=-\frac{1+e}{s_w(\lambda_s+\kappa_s)}d\varepsilon_v^{sp}-\frac{1+e}{(\lambda_s+\kappa_s)}\left(1-\frac{S}{S_{seg}}\right)d\varepsilon_v^{mp} \tag{3.15}$$

3.2.4 Flow rules

A non-associated flow rule is used for the LC yield surface, while an associated flow rule is employed for the GS yield surface

$$d\boldsymbol{\varepsilon}^{mp} = d\lambda_1 \frac{\partial Q_1}{\partial \boldsymbol{\sigma}^*} \tag{3.16}$$

$$d\boldsymbol{\varepsilon}^{sp} = -d\lambda_2 \frac{\partial F_2}{\partial S}\boldsymbol{I} \tag{3.17}$$

where $d\lambda_1$ and $d\lambda_2$ are the plastic multiplayers regarding to LC and SG yield surfaces, respectively, and Q_1 is the plastic potential function defined as

$$Q_1 = \left[p^* - \frac{\left(1+\gamma s_i\right) p_y^* - \left(1-\gamma s_i\right) k_t S}{2} \right]^2 + \left(\frac{q^*}{M} \right)^2 \tag{3.18}$$

where γ is a material parameter. It is worth reminding that the suction-induced plastic strain (equation 3.17) is the result of interfacial premelting mechanism.

3.3 Determination of the parameters

The proposed model requires ten parameters for describing the behavior under the variation of solid phase stress (G_0, κ_0, $E_{f_{ref}}$, $E_{f_{inc}}$, ν_f, γ, $p_{y_0}^*$, p_c^*, λ_0 and M), three parameters regarding to suction-induced strains (S_{seg}, λ_s and κ_s) and three parameters for coupling effects (β, r and k_t). Plotting the results of an isotropic drained compression test for an unfrozen state of the soil in $v:\ln p$ plane can provide the data to find the elastic compressibility coefficient, κ_0, the reference stress, p_c^*, the initial value of the preconsolidation stress, $p_{y_0}^*$, and the elastic-plastic compressibility coefficient, λ_0. A normal drained shear strength test at an unfrozen state of the soil can be used for determining the elastic shear modulus of the soil in unfrozen state, G_0, and also for the slope of the critical state line, M.

Conducting an unconfined triaxial compression test in an arbitrary reference temperature at a frozen state of the soil, can be used for determining the reference Young's modulus of the frozen soil, $E_{f_{ref}}$. Similar test in a different negative temperature can be considered to find $E_{f_{inc}}$. Then, an isotropic compression test at a frozen state of the soil with a certain value of ice saturation can be used for calculating the Poisson's ratio of the soil in the fully frozen state, ν_f, using equation (3.3).

The parameter k_t which controls the increase of apparent cohesion with cryogenic suction can be calculated based on the result of a drained shear stress test at a frozen state of the soil, using the following equation

$$q_f^* = M(p_f^* + k_t S) \tag{3.19}$$

where q_f^* and p_f^* denote the deviatoric and mean solid phase stresses at the critical state of the frozen soil. Considering equation (3.8), β and r can be calculated by determining λ at two different frozen states of the soil. Then, the parameter γ can be found using a trial-and-error procedure to fit the volumetric behavior of the soil at two different frozen states. Finally, the result of a test involving a freezing-thawing cycle plotted in $v:\ln(\mathrm{S}+\mathrm{p}_{at})$ plane is required to determine the values of S_{seg}, λ_s and κ_s.

3.4 Model results

In order to examine the ability of the model to simulate the behavior of frozen soils in an acceptable way, two different series of triaxial compression tests are simulated and compared with model predictions. Moreover, since experimental data is still limited, model results for an ice segregation phenomenon and also for strength weakening due to pressure melting are presented and discussed at a qualitative level.

3.4.1 Influence of temperature

Xu [9] reported a series of triaxial compression tests conducted on frozen sand specimens at initial confining pressure of 1 MPa, constant strain rate of 1.67E-4 s^{-1} and different temperatures of -1, -2, -5 and -10^o C. Since the values of suction were not reported, for the simulations, the Clausius-Clapeyron equation with $l = 334\ \mathrm{MJ/ton}$ and $\rho_i = 0.9\ \mathrm{ton/m^3}$ is used to evaluate the values of suction at the different temperatures. The obtained corresponding suctions, for the samples at -1, -2, -5 and -10^o C, are 1.016, 2.036, 5.118 and 10.326 MPa, respectively. The samples were frozen very quickly, so ice segregation was completely avoided. Considering the nature of sandy soils which cannot keep significant amount of unfrozen water below the freezing temperature, $\boldsymbol{\sigma} = \boldsymbol{\sigma}^*$ is assumed in the simulations. The initial void ratio of 0.4 is considered for the tests. The material parameters that are used to predict the soil behavior are listed in table 3.1.

Figure 3.4 shows a comparison of test data and model predictions for these tests. As shown in the figure, the model can successfully follow the trend of the behavior, however, lower and higher strength is predicted for the tests at -2^o C and -10^o C, respectively. As mentioned earlier, due to limitation of experimental data, some of the constitutive equations are borrowed from the BBM which is originally proposed for unsaturated soils (for instance the definition of the LC yield surface in $p^*:S$ plane and the linear expression for the increase in apparent cohesion). Hence, specifying appropriate mathematical expressions to describe the LC yield surface in $p^*:S$ plane and the increase in apparent cohesion, when more experimental data become available, will improve the results.

Table 3.1 Model parameters for frozen sand (influence of temperature)

Unfrozen soil shear modulus, MPa	$G_0 = 3.5$
Unfrozen soil elastic compressibility coefficient	$\kappa_0 = 0.07$
Frozen Soil Young's modulus at $T_{ref} = 273.16$ K , MPa	$E_{f_{ref}} = 200$
Rate of change in Young's modulus with temperature, MPa/K	$E_{f_{inc}} = 80$
Frozen Soil Poisson's ratio	$\nu_f = 0.31$
Plastic potential parameter	$\gamma = 0.06$
Initial preconsolidation stress for unfrozen state, MPa	$(p^*_{y_0})_{\text{in}} = 5.55$
Reference stress, MPa	$p^*_c = 0.1$
Elastic-plastic compressibility coefficient for unfrozen state	$\lambda_0 = 0.85$
Slope of the critical state line	$M = 1.52$
Initial segregation threshold, MPa	$(S_{seg})_{\text{in}} = 15$
Elastic compressibility coefficient for suction variation	$\kappa_s = 0.008$
Elastic-plastic compressibility coefficient for suction variation	$\lambda_s = 0.4$
Rate of change in apparent cohesion with suction	$k_t = 0.15$
Coefficient related to the maximum soil stiffness	$r = 0.66$
Rate of change in soil stiffness with suction, MPa^{-1}	$\beta = 0.11$

Table 3.2 Model parameters for frozen sand (influence of confining pressure)

Unfrozen soil shear modulus, MPa	$G_0 = 4.2$
Unfrozen soil elastic compressibility coefficient	$\kappa_0 = 0.03$
Frozen Soil Young's modulus at $T_{ref} = 273.16$ K , MPa	$E_{f_{ref}} = 30$
Rate of change in Young's modulus with temperature, MPa/K	$E_{f_{inc}} = 10$
Frozen Soil Poisson's ratio	$\nu_f = 0.48$
Plastic potential parameter	$\gamma = 0.01$
Initial preconsolidation stress for unfrozen state, MPa	$(p^*_{y_0})_{\text{in}} = 4.2$
Reference stress, MPa	$p^*_c = 0.47$
Elastic-plastic compressibility coefficient for unfrozen state	$\lambda_0 = 0.2$
Slope of the critical state line	$M = 1.17$
Initial segregation threshold, MPa	$(S_{seg})_{\text{in}} = 15$
Elastic compressibility coefficient for suction variation	$\kappa_s = 0.008$
Elastic-plastic compressibility coefficient for suction variation	$\lambda_s = 0.4$
Rate of change in apparent cohesion with suction	$k_t = 0.09$
Coefficient related to the maximum soil stiffness	$r = 0.59$
Rate of change in soil stiffness with suction, MPa^{-1}	$\beta = 0.09$

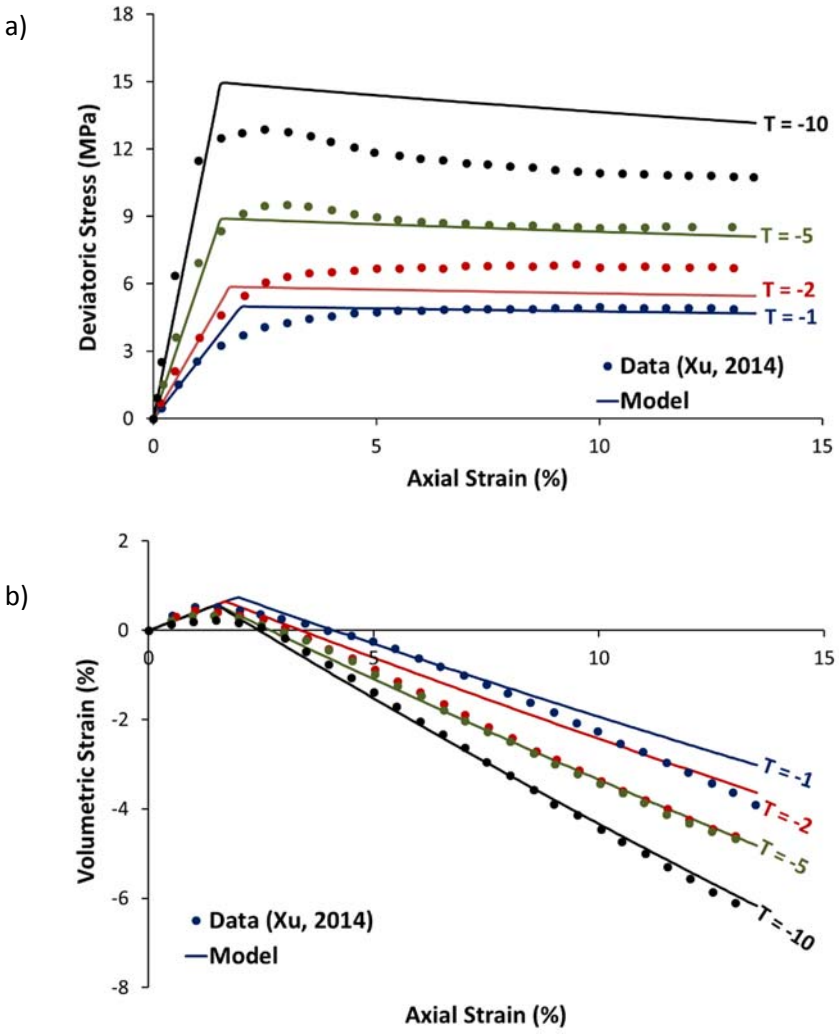

Fig 3.4. Comparison between the measured and predicted results for triaxial tests under different temperatures: (a) stress-strain relation and (b) volumetric strain

3.4.2 Influence of confining pressure

Triaxial compression tests on another type of frozen sands at different confining pressures of 0.3, 0.6, 0.8 and 1 MPa are also reported by Xu [9]. The tests were conducted at -4 and -6^{o} C with the constant strain rate of 1.67E-4 s^{-1}. Similar to the previous example, the obtained corresponding suctions, for the samples at -4 and -6^{o} C, are 4.087 and 6.152 MPa, respectively. The samples were prepared with the same conditions as the previous example, so the assumption of $\sigma = \sigma^{*}$ is also considered here. The initial void ratio of 0.3 is considered for these samples. The material parameters are listed in table 3.2. Comparative results are presented in figures 3.5 and 3.6.

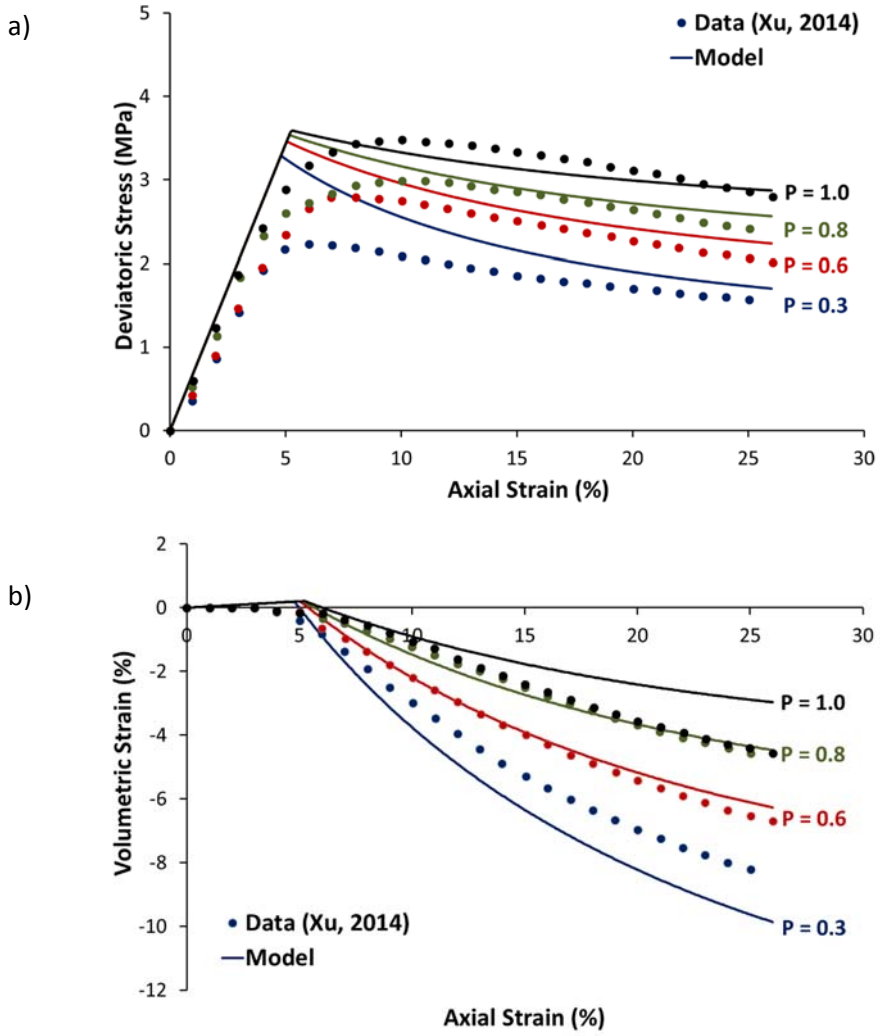

Fig 3.5. Comparison between the measured and predicted results for triaxial tests at different confinements at -4° C: (a) stress-strain relation and (b) volumetric strain

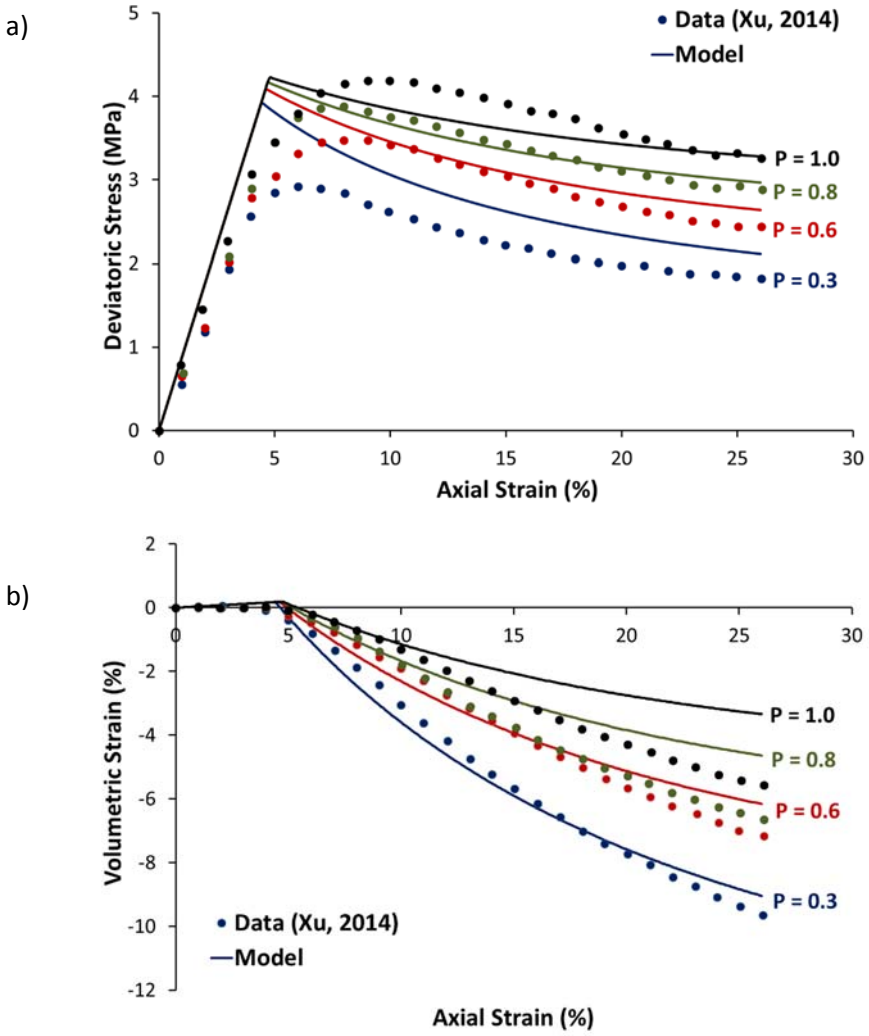

Fig 3.6 Comparison between the measured and predicted results for triaxial tests at different confinements at -6° C: (a) stress-strain relation and (b) volumetric strain

3.4.3 Ice segregation

In this section, the ability of the model to simulate an ice segregation phenomenon is described qualitatively. In this regard, a silt sample with the set of parameters listed in table 3.3 is considered to be freezed under the temperature variation of +1 to -4° C. The initial value of void ratio is 0.3 and the sample is initially subjected to a hydrostatic pressure of 0.3 MPa.

Silt can keep significant amount of unfrozen water during a normal freezing period, and also its relatively high permeability can allow water to be sucked into the freezing fringe. Considering these properties, a logical stress path and unfrozen water variation (figure 3.7) are assumed to be applied on the sample. The simulation predicts significant volume expansion for this simulation (figure 3.8). As shown in the figure, for the earlier stage of freezing, when the behavior is dominated by the effect of

curvature-induced premelting mechanism, stress state is located in the elastic region. Further freezing causes the sample to yield on the GS surface. From this point, interfacial permelting is the dominant mechanism and ice segregation phenomenon is expected. This results in a significant volume expansion and a softer behavior of the soil. Figure 3.7 shows the initial and final positions of the yield surfaces in $p^* : S$ plane. As shown in the figure, an inward movement of LC, which is the indication of strength weakening, is predicted. Further continuation of temperature reduction results in lower and lower value of unfrozen water saturation and its relative permeability. Hence, the rate of expansion are expected to be decreased by decreasing water saturation. This behavior is also predicted by the model (figure 3.8).

To investigate the capability of the model to simulate the behavior after grain segregation, the simulation is then followed by deviatoric loading. The selected parameters results in contractive behavior of the soil (figure 3.9). Higher value of preconsolidation stress would results in dilative behavior. Dilative behavior is simulated by assuming $p^*_{y_0} = 2.15$ MPa, as shown in figure 3.9.

Table 3.3 Model parameters for silt under a freezing period

Unfrozen soil shear modulus, MPa	$G_0 = 4.2$
Unfrozen soil elastic compressibility coefficient	$\kappa_0 = 0.03$
Frozen Soil Young's modulus at $T_{ref} = 273.16$ K , MPa	$E_{f_{ref}} = 50$
Rate of change in Young's modulus with temperature, MPa/K	$E_{f_{inc}} = 10$
Frozen Soil Poisson's ratio	$\nu_f = 0.4$
Plastic potential parameter	$\gamma = 0.1$
Initial preconsolidation stress for unfrozen state, MPa	$(p^*_{y_0})_{\text{in}} = 1.15$
Reference stress, MPa	$p^*_c = 0.1$
Elastic-plastic compressibility coefficient for unfrozen state	$\lambda_0 = 0.85$
Slope of the critical state line	$M = 1.22$
Initial segregation threshold, MPa	$(S_{seg})_{\text{in}} = 0.7$
Elastic compressibility coefficient for suction variation	$\kappa_s = 0.02$
Elastic-plastic compressibility coefficient for suction variation	$\lambda_s = 1.3$
Rate of change in apparent cohesion with suction	$k_t = 0.09$
Coefficient related to the maximum soil stiffness	$r = 0.75$
Rate of change in soil stiffness with suction, MPa^{-1}	$\beta = 1.7$

a)

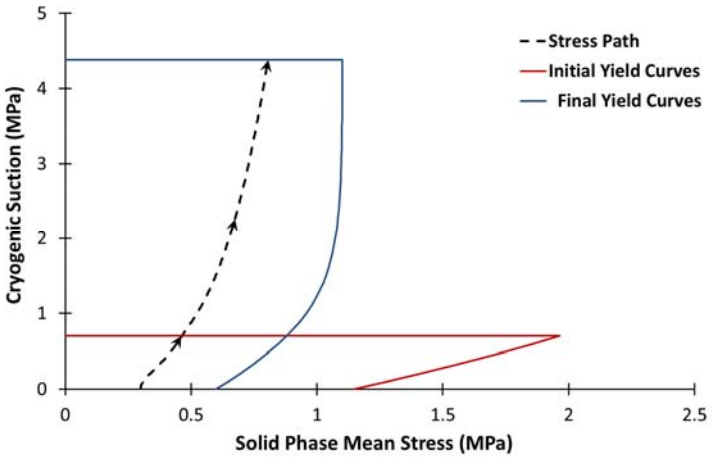

b)

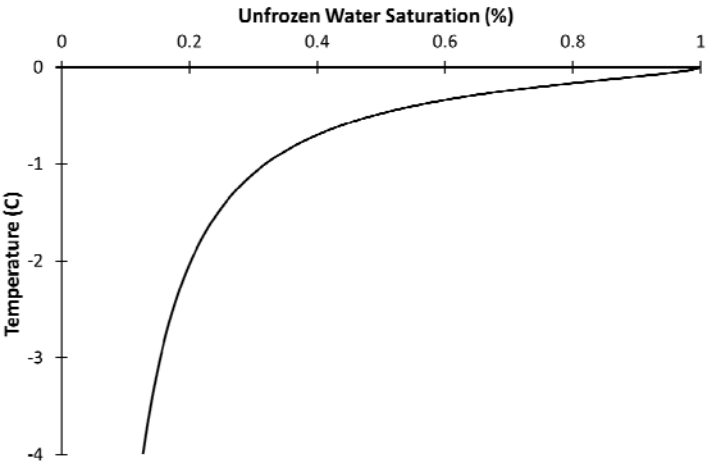

Fig 3.7 Loading conditions for ice segregation simulation: (a) stress path and (b) unfrozen water saturation

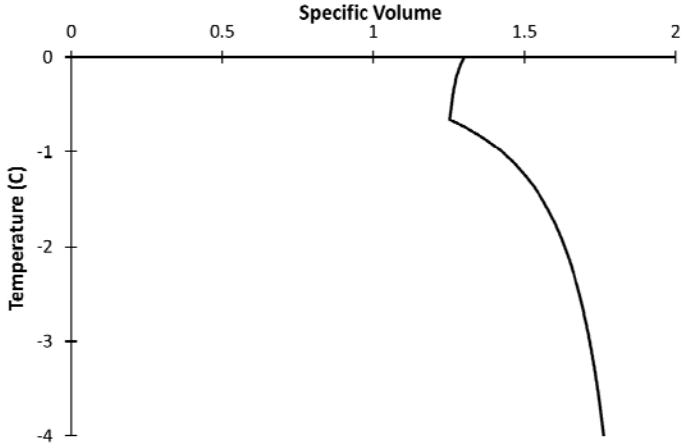

Fig 3.8 Volume change during a freezing period of a slit sample

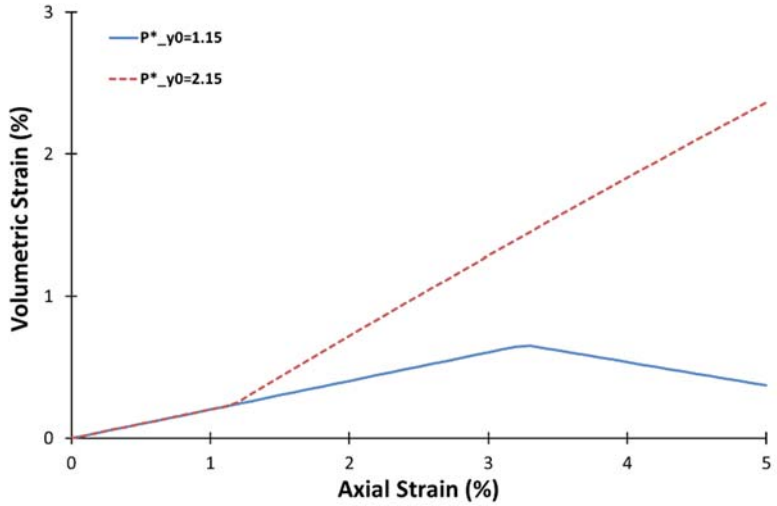

Fig 3.9 Volumetric behavior of the soil after ice segregation

3.4.4 Pressure Melting

High confining pressure results in pressure melting of ice crystals due to reduction of the thawing temperature. So, higher value of unfrozen water saturation is expected. As a result, the soil will experience strength weakening. In order to examine the ability of the model in simulation of this behavior, an undrained triaxial test on a soil sample with the set of parameters listed in table 3.4 is assumed. The initial value of void ratio and confining pressure are assumed to be equal to 0.3 and 5 MPa, respectively. A constant temperature of -1^{o} C is considered during the simulation. In this simulation, the following expression is considered for the thawing temperature of ice (T_0)

$$T_0 = 273.16\left(\frac{p_w + S}{-395} + 1\right)^{\frac{1}{9}} \qquad (3.20)$$

where T_0 is in Kelvin and p_w and S are in MPa.

During the simulation of the pressure melting phenomenon, a reduction of cryogenic suction from 1.02 to 0.09 MPa is experienced in the sample simultaneously with the axial deformation. The resulting stress-strain curve is presented in figure 3.10. As expected, softening behavior is predicted by the model. Figure 3.11 shows the stress path and the corresponding positions of yield curves at the initial and final stages of the simulation in $p^*:\mathrm{S}$ and $p^*:q^*$ planes. As shown in the figure, stress state is located on the wet side of the critical state line, so the LC yield surface moves outward. At the same time, due to suction decrease, the apparent preconsolidation stress reduces, and the size of yield surface in $p^*:q^*$ plane shrinks. Total behavior is the combination of these two mechanisms.

Table 3.4 Model parameters for pressure melting

Unfrozen soil shear modulus, MPa	$G_0 = 3.5$
Unfrozen soil elastic compressibility coefficient	$\kappa_0 = 0.03$
Frozen Soil Young's modulus at $T_{ref} = 273.16$ K , MPa	$E_{f_{ref}} = 50$
Rate of change in Young's modulus with temperature, MPa/K	$E_{f_{inc}} = 10$
Frozen Soil Poisson's ratio	$\nu_f = 0.4$
Plastic potential parameter	$\gamma = 0.01$
Initial preconsolidation stress for unfrozen state, MPa	$(p^*_{y_0})_{\text{in}} = 5.85$
Reference stress, MPa	$p^*_c = 0.07$
Elastic-plastic compressibility coefficient for unfrozen state	$\lambda_0 = 0.7$
Slope of the critical state line	$M = 1.22$
Initial segregation threshold, MPa	$(S_{seg})_{\text{in}} = 2$
Elastic compressibility coefficient for suction variation	$\kappa_s = 0.008$
Elastic-plastic compressibility coefficient for suction variation	$\lambda_s = 0.4$
Rate of change in apparent cohesion with suction	$k_t = 0.09$
Coefficient related to the maximum soil stiffness	$r = 0.49$
Rate of change in soil stiffness with suction, MPa^{-1}	$\beta = 0.17$

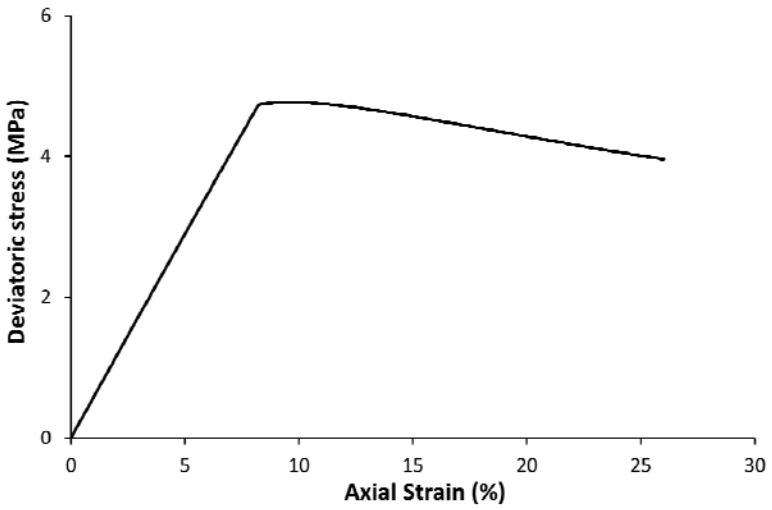

Fig 3.10 Stress-stain behavior due to pressure melting

a)

b)

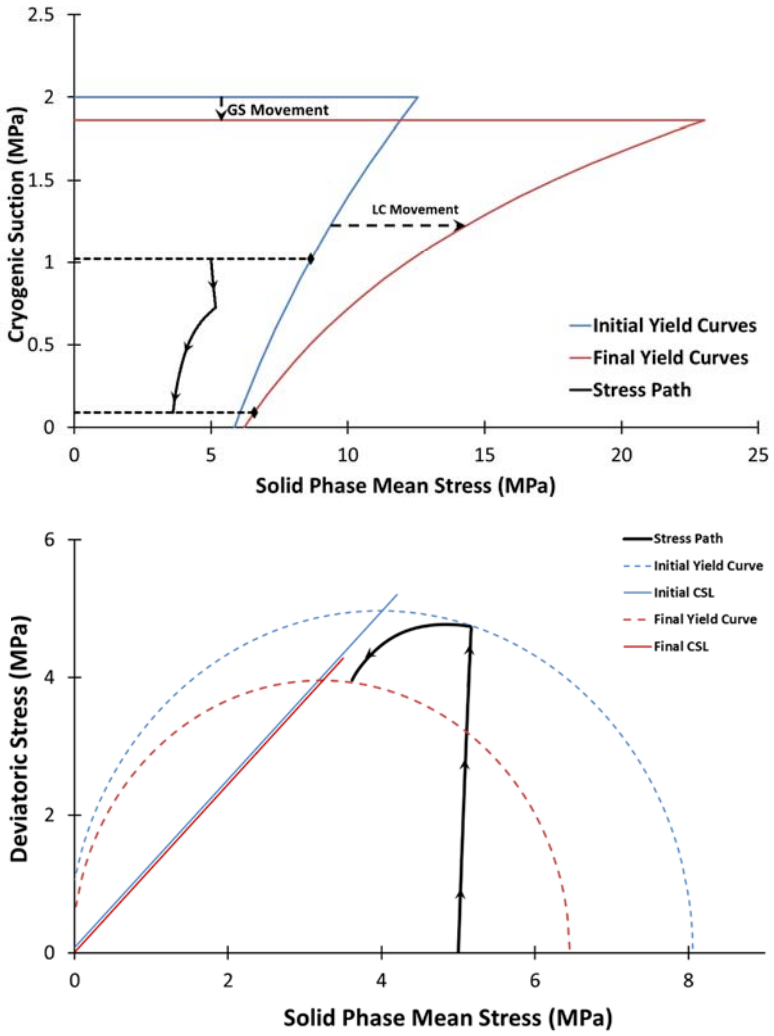

Fig 3.11 Stress path, initial and final positions of the yield surfaces due to pressure melting: (a) in $p^*:S$ plane and (b) in $p^*:q^*$ plane

4 Elastic-viscoplastic model

4.1 Strain decomposition

Similar to the elastic-plastic model, any strain increment is decomposed into two major parts due to variations of solid phase stress and suction. In this model, elastic-viscoplastic behavior is considered for the deformation due to variation of solid phase stress, while elastic-plastic behavior is assumed for the suction induced deformation. Thus, any strain increment, $d\boldsymbol{\varepsilon}$, can be additively decomposed into the following parts

$$d\boldsymbol{\varepsilon} = d\boldsymbol{\varepsilon}^{me} + d\boldsymbol{\varepsilon}^{se} + d\boldsymbol{\varepsilon}^{mvp} + d\boldsymbol{\varepsilon}^{sp} \tag{4.1}$$

where $d\boldsymbol{\varepsilon}^{me}$, $d\boldsymbol{\varepsilon}^{se}$ and $d\boldsymbol{\varepsilon}^{sp}$ are defined in section 3.1, and $d\boldsymbol{\varepsilon}^{mvp}$ indicates the viscoplastic part of strain due to the solid phase stress variation.

Similar to the previous chapters, compressive stress and strain are assumed to be positive.

4.2 Model formulation

4.2.1 Elastic response

For the elastic part of the model, similar formulation to section 3.2.1 is considered.

4.2.2 Reference, dynamic and yield surfaces

As mentioned in section 4.1, in this model, elastic-plastic behavior is assumed for the suction induced deformation. Thus, a similar yield curve with the one introduced in equation (3.9) is considered here for the GS curve.

The viscoplastic part of the model is developed based on the overstress framework, originally proposed by Perzyna [45], and the elastic-plastic model described in the previous chapter. In the overstress method, instead of the common yield surface, reference and dynamic surfaces should be defined. Then, the inelastic part of deformation can be calculated based on the distance of the reference and dynamic surfaces.

Based on the proposed elastic-plastic model, the LC reference surface is introduced as

$$F_r = \left[p_r^* - \left(\frac{p_{yr}^* + p_{tr}^*}{2} \right) \right]^2 + \left(\frac{q_r^*}{M} \right)^2 - \left(\frac{p_{yr}^* - p_{tr}^*}{2} \right)^2 = 0 \tag{4.2}$$

where

$$p_{yr}^* = p_c^* \left(\frac{p_{y_{0r}}^*}{p_c^*} \right)^{\frac{\lambda_0 - \kappa}{\lambda - \kappa}} \tag{4.3}$$

and (p_r^*, q_r^*) indicates the stress point on the LC reference surface, $p_{y_{0r}}^*$ and p_c^* are the preconsolidation stress and the reference stress for unfrozen condition corresponding to the reference strain rate, p_{tr}^* is defined in figure 4.1 and the other parameters are defined in section 3.2.2.

The LC dynamic surface should always pass through the current stress point (p^*, q^*, S) and also keeps a similar shape to the LC reference surface with respect to a similarity line (or the corresponding similarity center in the $p^* - q^*$ space). In this model, the line $S = 0$ is considered as the similarity line. This results in the following geometrical properties:

1- All lines connecting an arbitrary point like (p^*, q^*, S) on the LC dynamic surface and its conjugated point on the LC reference surface join at the ($0, 0, S$).
2- All ratios of the distance of any arbitrary point like (p^*, q^*, S) on the LC dynamic surface from the similarity center, ($0, 0, S$), to the distance of its conjugated point on the LC reference surface from the similarity center, ($0, 0, S$), are identical. This ratio is called the similarity ratio, R , and coincides with the ratio of the sizes of these surfaces.

The LC dynamic surface can then be described as

$$F_d = \left[p^* - \left(\frac{p_{yd}^* + p_{td}^*}{2} \right) \right]^2 + \left(\frac{q^*}{M} \right)^2 - \left(\frac{p_{yd}^* - p_{td}^*}{2} \right)^2 = 0 \tag{4.4}$$

where

$$p_{yd}^* = R \,.\, p_{yr}^* \tag{4.5}$$

$$p_{td}^* = R \,.\, p_{tr}^* \tag{4.6}$$

4.2.3 Hardening rules

Similar hardening rules to section 3.2.3 are considered here for $p_{y_{0r}}^*$ and S_{seg}

$$\frac{dp_{y_{0r}}^*}{p_{y_{0r}}^*} = \frac{1+e}{\lambda_0 - \kappa_0} d\varepsilon_v^{mvp} + \frac{1+e}{\lambda_0 - \kappa_0} d\varepsilon_v^{sp} \tag{4.7}$$

$$\frac{dS_{seg}}{S_{seg} + p_{at}} = -\frac{1+e}{s_w (\lambda_s + \kappa_s)} d\varepsilon_v^{sp} - \frac{1+e}{(\lambda_s + \kappa_s)} \left(1 - \frac{S}{S_{seg}} \right) d\varepsilon_v^{mvp} \tag{4.8}$$

In addition, considering the description in section 2.1.4, the bonds between soil grains and ice crack with developing shear strain. On the other hand, these bonds will recover and be stronger by increasing suction. Thus, the following hardening rule is suggest for p_{tr}^*

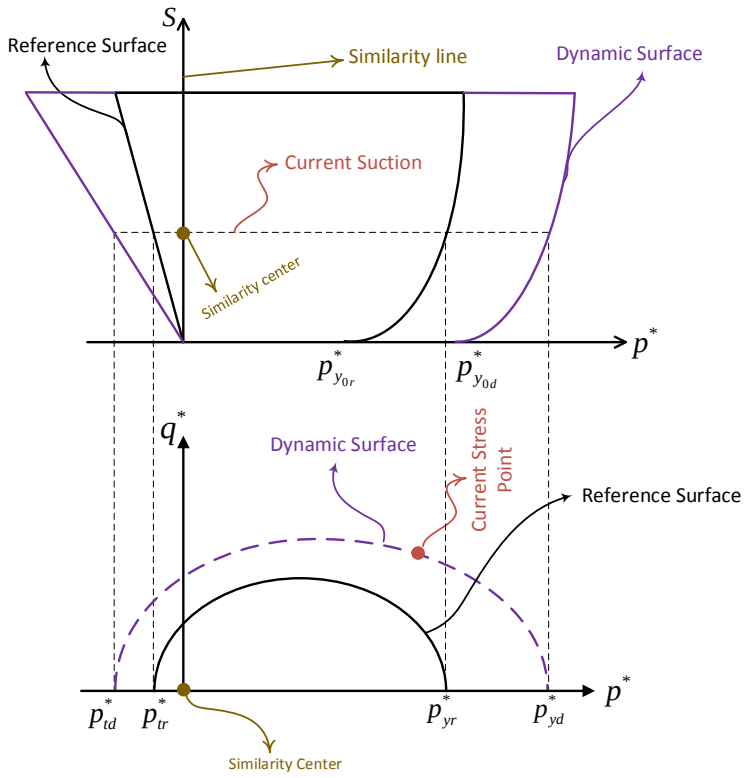

Figure 4.1 Reference, dynamic and yield curves for elastic-viscoplastic model

$$\frac{dp^*_{tr}}{p^*_{tr}} = -k_{t_1}\frac{dS}{p^*_{tr}}\left(H(-p^*_{tr})\times H(dS)\right) - k_{t_2}.d\varepsilon_q^{mvp} \tag{4.9}$$

where k_{t_1} and k_{t_2} are model parameters, and H is the Heaviside function

$$H(x) = \begin{cases} 0 & x \le 0 \\ 1 & x > 0 \end{cases} \tag{4.10}$$

4.2.4 Flow rules

For the suction induced plastic strain, $d\varepsilon^{sp}$, similar flow rule to section 3.2.4 is considered, while the viscoplastic part of the strain increment due to variation of solid phase stress is calculated based on the similarity ratio

$$d\boldsymbol{\varepsilon}^{mvp} = \mu\left\langle R^N\right\rangle\frac{\partial Q_1}{\partial \boldsymbol{\sigma}^*}.dt = \Delta\lambda_1 \times \frac{\partial Q_1}{\partial \boldsymbol{\sigma}^*} \tag{4.11}$$

where, $\langle\ \rangle$ is the Macaulay brackets, dt is the time increment, μ stands for the fluidity of the system corresponding to the reference strain rate, N is the strain rate coefficient and Q_1 is the plastic potential function

$$Q_1 = \left[p^* - \frac{\left(1+\gamma s_i\right) p_{yd}^* + \left(1-\gamma s_i\right) p_{td}^*}{2} \right]^2 + \left(\frac{q^*}{M} \right)^2 \tag{4.12}$$

In common unfrozen soils, μ and N are considered as constant parameters, while in frozen soils this assumption should be examined more precisely. Thus, we can consider the concept of these parameters in a simple 1D model. In the overstress method, the main idea is to calculate the plastic strain rate for the reference strain rate, $\dot{\varepsilon}_v^r$, and then to scale it to the current rate (see figure 4.2)

$$\dot{\varepsilon}_v^{\ vp} = \dot{\varepsilon}_v^{\ r} \frac{\lambda - k}{\lambda} \left(\frac{p_{cd}}{p_{cr}} \right)^N = \mu \left(\frac{p_{cd}}{p_{cr}} \right)^N \tag{4.13}$$

As shown in the figure, assuming constant slopes for the lines in $\varepsilon_v - \ln \sigma_v'$ plane (i.e. λ) and in $\ln \dot{\varepsilon}_v - \ln \sigma_v'$ plane (i.e. N) for different strain rates is crucial in this concept. On the other hand, the parameter μ actually carries the reference strain rate ($\dot{\varepsilon}_v^r$), κ and λ, where all of them are considered to be constant. However, in frozen states, κ and λ is varying with ice content, temperature and cryogenic suction. Thus, we need to transfer the reference curve to the current state of ice content, temperature and suction to be able to scale the plastic strain rate from the reference rate to the current rate (see figure 4.3). This can simply considered as

$$\dot{\varepsilon}_v^{\ mvp} = \dot{\varepsilon}_v^{\ r} \frac{\lambda - k}{\lambda} \left(\frac{p_{yd}^*}{p_{yr}^*} \right)^{N_s} = \mu_0 \frac{\lambda_0 \left(\lambda - k\right)}{\lambda \left(\lambda_0 - k_0\right)} \left(\frac{p_{yd}^*}{p_{yr}^*} \right)^{N_s} \tag{4.14}$$

So, μ could be defined as

$$\mu = \mu_0 \frac{\lambda_0 \left(\lambda - k\right)}{\lambda \left(\lambda_0 - k_0\right)} \tag{4.15}$$

where μ_0 is the fluidity of unfrozen soil for the reference strain rate.

On the hand, we know that rate dependency of an unfrozen sample is less than a frozen sample. So, lower value of strain rate coefficient, N, for higher ice content is expected. However, rate dependency of ice decreases with decreasing temperature. Thus, higher value of N for higher suction should be expected. These dependencies of N could be considered as

$$N = N_0 + b_1 \times S - b_2 \times s_i \tag{4.16}$$

where N_0 is the strain rate coefficient of unfrozen soil, and b_1 and b_2 are two model parameters.

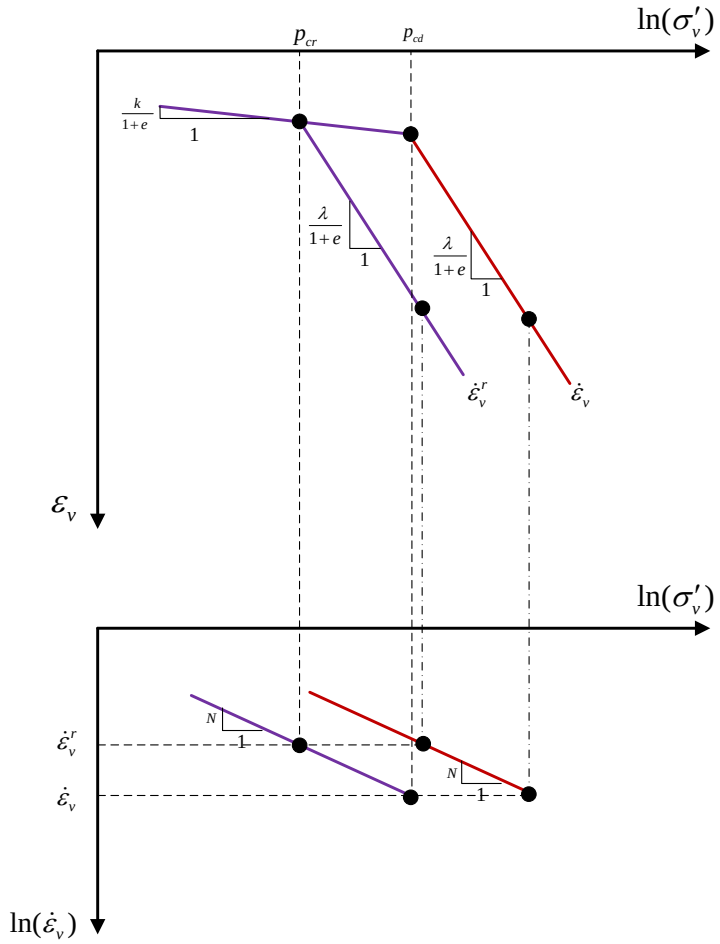

Figure 4.2 Schematic representation of 1D overstress framework for unfrozen soils

4.3 Determinations of the parameters

The proposed model requires ten parameters for describing the behavior under the variation of solid phase stress (G_0, κ_0, $E_{f_{ref}}$, $E_{f_{inc}}$, ν_f, γ, $p^*_{y_{0r}}$, p^*_c, λ_0 and M), three parameters regarding to suction-induced strains (S_{seg}, λ_s and κ_s), four parameters for coupling effects (β, r, k_{t_1} and k_{t_2}) and four parameters for rate effects (μ_0, N_0, b_1 and b_2). The first three groups of the parameters, except k_{t_1} and k_{t_2}, can be determined similar to the procedure described in section 3.3. Note that the parameters $p^*_{y_{0r}}$ and p^*_c should be determined with respect to the reference strain rate.

The viscous parameters for the unfrozen state, μ_0 and N_0, can be determined in a common way from oedometer tests at a constant strain rate or from a conventional oedometer test. Evaluating N in two different frozen states with certain values of cryogenic suction and ice content will provide required data to find b_1 and b_2.

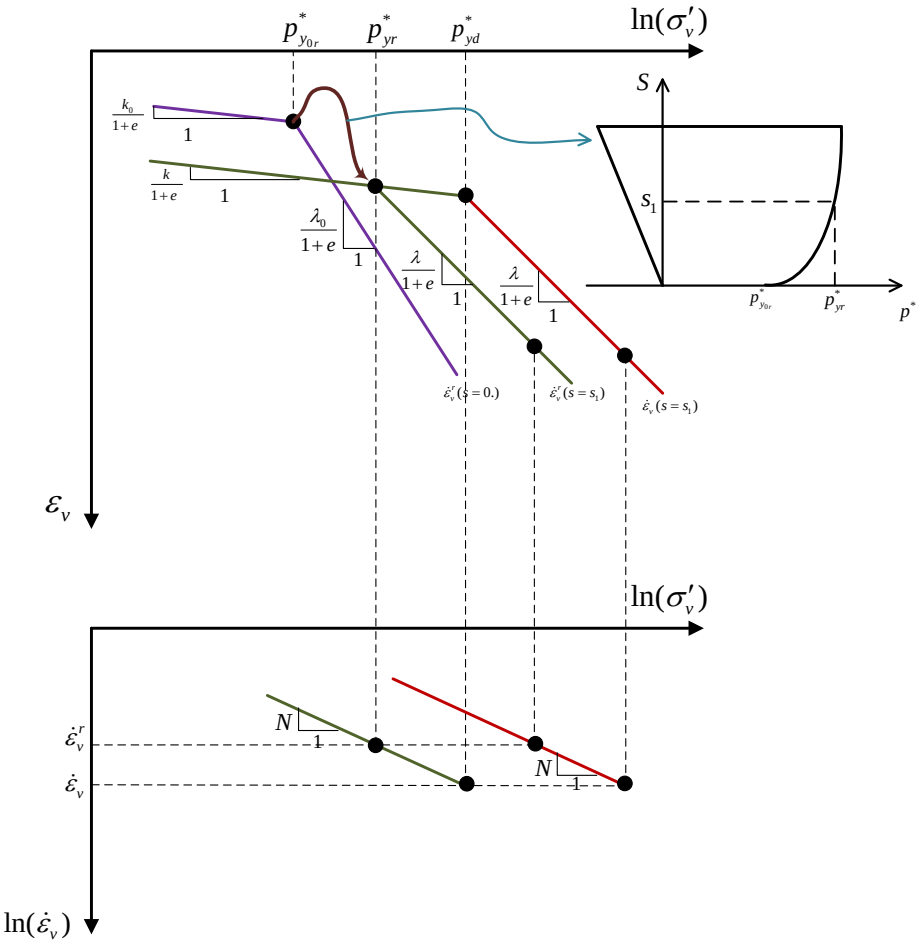

Figure 4.3 Schematic 1D representation of the overstress framework for frozen soils

The parameters k_{t_1} and k_{t_2} can be determined using a trial-and-error procedure to fit the time to failure curves of the soil in two different frozen states.

4.4 Model Results

4.4.1 Uniaxial compression tests at different strain rates

Zhu and Carbee [46] conducted some uniaxial compression tests on frozen Fairbanks silt. The soil tested has 34.2% of plastic limit and 38.4% of liquid limit. The samples were first reached to the desired density by compressing them in acrylic plastic molds with the dimensions of 70 mm in diameter and 152 mm in length. After the specimens were saturated with a vacuum pump, they were placed into a freezing cabinet and frozen quickly to avoid ice lens during freezing. Four different strain rates of 1.1E-3, 1.1 E-4, 1.1E-5 and 1.1E-6 s^{-1} at -3° C are considered in this section for verification of the model. The initial void ratio of 0.3 is considered for the tests. The material parameters that are used to predict the soil behavior are listed in table 4.1. Comparative results are presented in figure 4.4.

Table 4.1 Model parameters for frozen Fairbanks silt

Unfrozen soil shear modulus, MPa	$G_0 = 5$
Unfrozen soil elastic compressibility coefficient	$\kappa_0 = 0.03$
Frozen Soil Young's modulus at $T_{ref} = 273.16$ K , MPa	$E_{f_{ref}} = 140$
Rate of change in Young's modulus with temperature, MPa/K	$E_{f_{inc}} = 10$
Frozen Soil Poisson's ratio	$\nu_f = 0.48$
Plastic potential parameter	$\gamma = 0.01$
Initial preconsolidation stress for unfrozen state, MPa	$(p^*_{y_{0r}})_{\text{in}} = 0.9$
Reference stress, MPa	$p^*_c = 0.07$
Elastic-plastic compressibility coefficient for unfrozen state	$\lambda_0 = 0.7$
Slope of the critical state line	$M = 1.05$
Initial segregation threshold, MPa	$(S_{seg})_{\text{in}} = 10$
Elastic compressibility coefficient for suction variation	$\kappa_s = 0.008$
Elastic-plastic compressibility coefficient for suction variation	$\lambda_s = 0.4$
Rate of change in apparent cohesion with suction	$k_{t_1} = 0.3$
Hardening parameter for apparent cohesion	$k_{t_2} = 1.5$
Coefficient related to the maximum soil stiffness	$r = 0.49$
Rate of change in soil stiffness with suction, MPa^{-1}	$\beta = 0.15$
Fluidity parameter for unfrozen state, s^{-1}	$\mu_0 = 2E-6$
Rate dependency parameter for unfrozen state	$N_0 = 25$
Rate of change in N with suction, MPa^{-1}	$b_1 = 0.58$
Rate of change in N with ice saturation	$b_2 = 22$

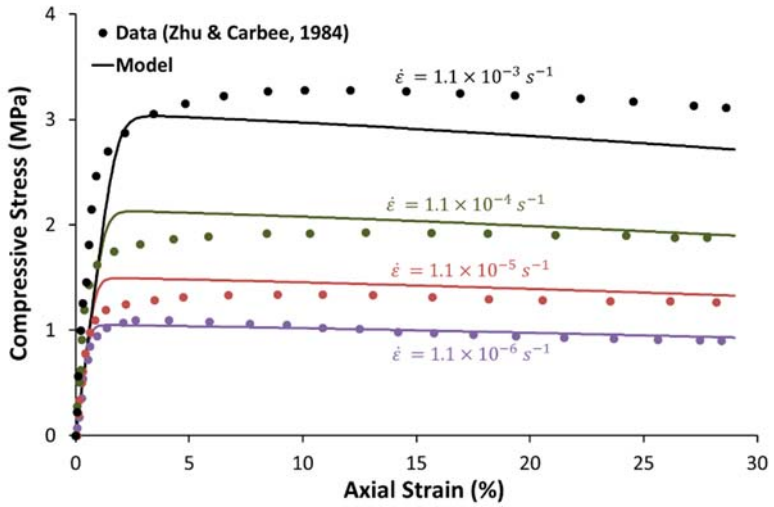

Figure 4.4 Comparison between the measured and predicted stress-strain curves for frozen Fairbanks silt (-3° C)

4.4.2 Creep tests at different temperatures and stress levels

We proceed to validate the model by simulating the creep tests conducted by Eckardt [47] at different temperature and stress levels . The samples tested were cohesionless sand with medium grain size d_{50}=0.4 mm, initial void ratio of 0.5 and dry density of 1750 kg/m^3. The samples had the dimensions of 100 mm in diameter and 200 mm in length. The tests were done in a cold room, with capability of adjusting temperature with high accuracy. In the tests, different temperatures (-5 and -15^o C) are concerned, depending on which, different creep stress, from lowest 1.0 MPa to highest 8.0 MPa, are also considered. Creep stress on samples from frozen, water saturated medium sand was kept constant through testing at different temperatures. The material parameters that are used to predict the soil behavior are listed in table 4.2. Comparative results are presented in figure 4.5.

Table 4.2 Model parameters for frozen sand (creep tests)

Unfrozen soil shear modulus, MPa	$G_0 = 5$
Unfrozen soil elastic compressibility coefficient	$\kappa_0 = 0.01$
Frozen Soil Young's modulus at $T_{ref} = 273.16$ K , MPa	$E_{f_{ref}} = 140$
Rate of change in Young's modulus with temperature, MPa/K	$E_{f_{inc}} = 10$
Frozen Soil Poisson's ratio	$\nu_f = 0.48$
Plastic potential parameter	$\gamma = 0.01$
Initial preconsolidation stress for unfrozen state, MPa	$(p^*_{y_{0r}})_{\text{in}} = 0.28$
Reference stress, MPa	$p^*_c = 0.05$
Elastic-plastic compressibility coefficient for unfrozen state	$\lambda_0 = 0.02$
Slope of the critical state line	$M = 0.85$
Initial segregation threshold, MPa	$(S_{seg})_{\text{in}} = 10$
Elastic compressibility coefficient for suction variation	$\kappa_s = 0.008$
Elastic-plastic compressibility coefficient for suction variation	$\lambda_s = 0.4$
Rate of change in apparent cohesion with suction	$k_{t_1} = 0.45$
Hardening parameter for apparent cohesion	$k_{t_2} = 2.5$
Coefficient related to the maximum soil stiffness	$r = 0.49$
Rate of change in soil stiffness with suction, MPa^{-1}	$\beta = 0.15$
Fluidity parameter for unfrozen state, hr^{-1}	$\mu_0 = 8E-6$
Rate dependency parameter for unfrozen state	$N_0 = 25$
Rate of change in N with suction, MPa^{-1}	$b_1 = 0.33$
Rate of change in N with ice saturation	$b_2 = 21.1$

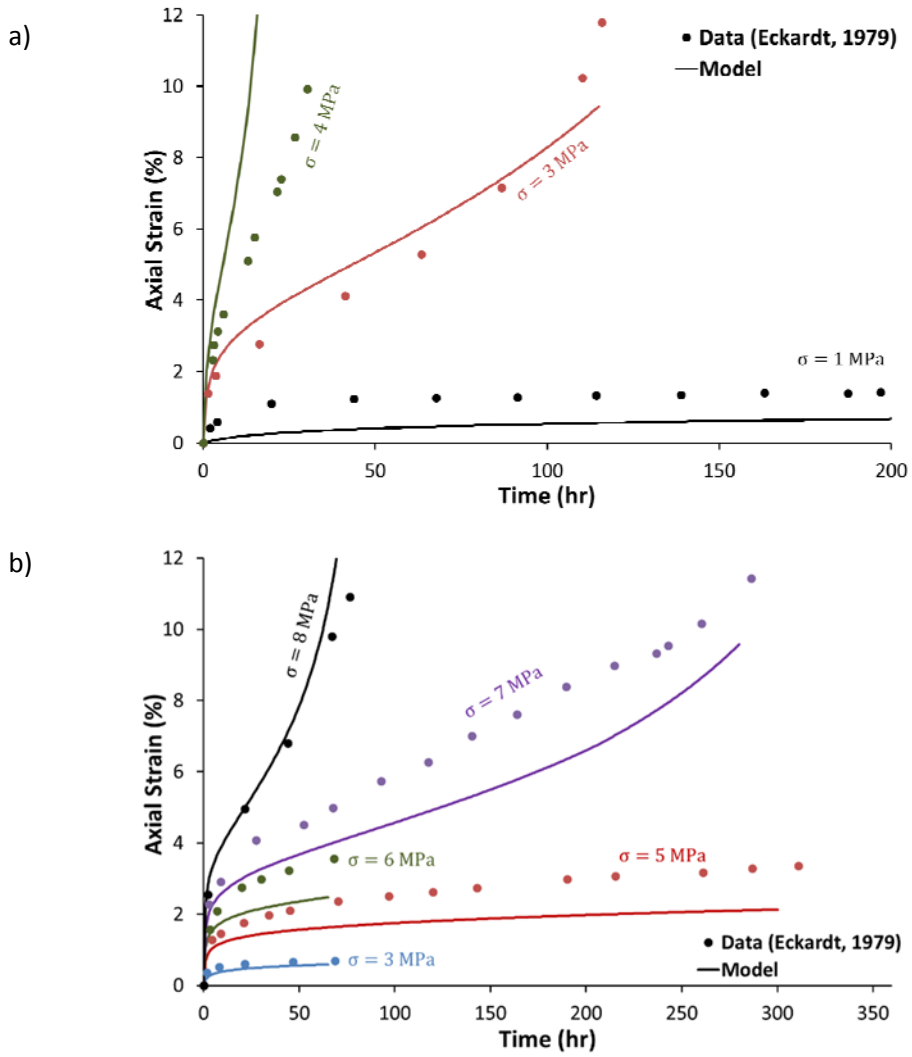

Figure 4.5 Comparison between the measured and predicted results for uniaxial creep tests at different stress level : (a) at -5° C and (b) at -15° C

5 Boundary value problem

5.1 Implementation

The elastic-viscoplastic model, introduced in chapter 4, is implemented into Plaxis using an implicit integration scheme. The user-defined subroutine takes in strains, cryogenic suction and time increments and gives out the solid phase stresses. The state of the soil is defined by the stress state and a set of state parameters.

The existence of a plastic yield surface (GS) together with a viscolpalstic reference/dynamic surface (LC) leads the model to two different integration algorithms for two different states.

It should be noted, since a combination of stress (suction) and strain increments is given as the input of the constitutive model, a mixed stress-strain-control procedure should be employed for the integration scheme.

5.1.1 Stress integration when GS is not active

Integrating the solid phase stress and other state variables requires the construction of the residual vector, $\boldsymbol{r}_1$, and the unknown vector, $\boldsymbol{x}_1$. Preliminarily, there are 8 unknown variables and equations for the solid phase stress vector, $\boldsymbol{\sigma}^*$, and the state parameters, $p^*_{y_{0r}}$ and p^*_{tr}. To reduce the nonlinearity of the system, 4 additional equations and unknowns: p^*_{yd}, p^*_{td}, R and $\Delta\lambda$, are added to the system of the equations.

$$\boldsymbol{x}_1 = \begin{bmatrix} \boldsymbol{\sigma}^* \\ p^*_{y_{0r}} \\ p^*_{tr} \\ \Delta\lambda_1 \\ p^*_{y_d} \\ p^*_{td} \\ R \end{bmatrix} ; \quad \boldsymbol{r}_1 = \begin{bmatrix} \Delta\boldsymbol{\sigma}^* - \boldsymbol{D}\left(\Delta\boldsymbol{\varepsilon} - \Delta\boldsymbol{\varepsilon}^{se} - \Delta\lambda_1 \times \dfrac{\partial Q_1}{\partial \boldsymbol{\sigma}^*}\right) \\ \Delta p^*_{y_{0r}} - \dfrac{dp^*_{y_{0r}}}{d\lambda_1}\Delta\lambda_1 \\ \Delta p^*_{tr} - \dfrac{dp^*_{tr}}{d\lambda_1}\Delta\lambda_1 \\ \Delta\lambda_1 - \dfrac{d\lambda_1}{dt}\Delta t \\ p^*_{y_d} - R\,.\,p^*_{yr} \\ p^*_{td} - R\,.\,p^*_{tr} \\ F_d \end{bmatrix} \tag{5.1}$$

5.1.2 Stress integration when GS is active

When suction meets the GS curve, the plastic constitutive equations for GS should be solved simultaneously with the viscoplastic constitutive equations for LC. In total, there are 14 unknown variables and equations for the solid phase stress vector, $\boldsymbol{\sigma}^*$, the state parameters: $p^*_{y_{0r}}$, S_{seg} and p^*_{tr}, and other required parameters: p^*_{yd}, p^*_{td}, R, $\Delta\lambda_1$ and $\Delta\lambda_2$.

$$\boldsymbol{x}_2 = \begin{bmatrix} \boldsymbol{\sigma}^* \\ p^*_{y_{0r}} \\ S_{seg} \\ p^*_{tr} \\ \Delta\lambda_1 \\ \Delta\lambda_2 \\ p^*_{y_d} \\ p^*_{td} \\ R \end{bmatrix}; \quad \boldsymbol{r}_2 = \begin{bmatrix} \Delta\boldsymbol{\sigma}^* - \boldsymbol{D}\left(\Delta\boldsymbol{\varepsilon} - \Delta\boldsymbol{\varepsilon}^{se} - \Delta\lambda_1 \times \dfrac{\partial Q_1}{\partial \boldsymbol{\sigma}^*} - \dfrac{\Delta\lambda_2}{3}\boldsymbol{I}\right) \\ \Delta p^*_{y_{0r}} - \dfrac{dp^*_{y_{0r}}}{d\lambda_1}\Delta\lambda_1 - \dfrac{dp^*_{y_{0r}}}{d\lambda_2}\Delta\lambda_2 \\ \Delta S_{seg} - \dfrac{dS_{seg}}{d\lambda_1}\Delta\lambda_1 - \dfrac{dS_{seg}}{d\lambda_2}\Delta\lambda_2 \\ \Delta p^*_{tr} - \dfrac{dp^*_{tr}}{d\lambda_1}\Delta\lambda_1 - \dfrac{dp^*_{tr}}{d\lambda_2}\Delta\lambda_2 \\ \Delta\lambda_1 - \dfrac{d\lambda_1}{dt}\Delta t \\ F_2 \\ p^*_{y_d} - R \,.\, p^*_{yr} \\ p^*_{td} - R \,.\, p^*_{tr} \\ F_d \end{bmatrix} \tag{5.2}$$

5.2 User manual

5.2.1 Installation

For recent versions of PLAXIS the two DLL files, udsm_pr.dll and udsm_pr64.dll, can be copied to the udsm folder within the main PLAXIS folder. The model can then be accessed by selecting “user-defined” when a new material is created.

5.2.2 Sign convention

Parameters are adopted with the sign convention of Plaxis. It means compressive stress and strain are assumed to be negative.

5.2.3 Parameters

In addition to the parameters of the mechanical constitutive model previously described in chapter 4, some additional parameters are also required for the global coupled FEM solution. The parameters and their description are listed in table 5.1.

5.3 Test case

Zhang et al. [48] conducted a long-term plate loading experiment (figure 5.1) in Beiluhe Basin on the Qinghai–Tibetan Plateau, which has an altitude of approximately 4618 m above sea level. From 2006 to 2014, the test platform was step-loaded three times: 0.09 MPa in September 2006, 0.19 MPa in August 2009 and 0.29 MPa in September 2010. The soil consists of silty sand over-laying silty clay and highly weathered mudstone (figure 5.2). The permafrost table occurs at a depth of 2-3 m, and ice-rich frozen soils are found beneath the permafrost table. The mean annual ground temperature varies between -0.5 and -1.8 ^{o} C.

Table 5.1 Input parameters

Symbol	Description
Model-ID	An ID for some internal adoption in PLAXIS. It should set to 15211522
Temp_Ref	Reference temperature for the elastic behavior of frozen soil
E_{fRef}	Young's modulus of frozen soil at the reference temperature
E_{fIncr}	Rate of change in Young's modulus with temperature
ν_f	Poisson's ratio for fully frozen state
G_0	Shear modulus for unfrozen state
κ_0	Elastic compressibility coefficient for unfrozen state
p^*_c	Reference stress
λ_0	Elastic-plastic compressibility coefficient for unfrozen state
γ	Plastic potential parameter
K_{t1}	Rate of change in apparent cohesion with suction
M	Slope of the critical state line
λ_s	Elastic-plastic compressibility coefficient for suction variation
κ_s	Elastic compressibility coefficient for suction variation
r	Coefficient related to the maximum soil stiffness
β	Rate of change in soil stiffness with suction
λ_r	Material parameters for unfrozen water saturation* and relative permeability**
p_r	Material parameters for unfrozen water saturation*
α	Material parameter for freezing Temp***
Thawing $Temp_{Ref}$	Material parameter for freezing Temp*** (common value: 273.16 K)
Thawing $Press_{Ref}$	Material parameter for freezing Temp*** (common value: -395 MPa)
K_{t2}	Hardening parameter for apparent cohesion
μ_0	Fluidity parameter for unfrozen state
N_0	Rate dependency parameter for unfrozen state
b_1	Rate of change in N with suction
b_2	Rate of change in N with ice saturation
OCR	Over consolidation ratio****
Initial segregation suction	Initial value of S_{seg}
Initial void ratio	e_0
Min. Ini. P^*_{Y0R}	Minimum acceptable value for P^*_{Y0R} at its initial state****
P_{at}	Atmospheric pressure
K_w	Bulk modulus of water

$$^{*}\, s_w = \left\{ 1 + \left(\frac{S}{p_r} \right)^{\frac{1}{1-\lambda_r}} \right\}^{-\lambda_r}$$

$$^{**}\, k_{rw} = \sqrt{s_w} \left[1 - (1 - s_w^{1/\lambda})^{\lambda} \right]^2$$

$$^{***}\, T_0 = \left(\text{Thawing Temp}_{\text{ref}} \right) \times \left(\frac{p_i}{-\text{Thawing Press}_{\text{ref}}} + 1 \right)^{1/\alpha}$$

**** In the initialization part, initial value of P^*_{Y0R} is calculated based on OCR, but it cannot be lower than its minimum value (Min. Ini. P^*_{Y0R})

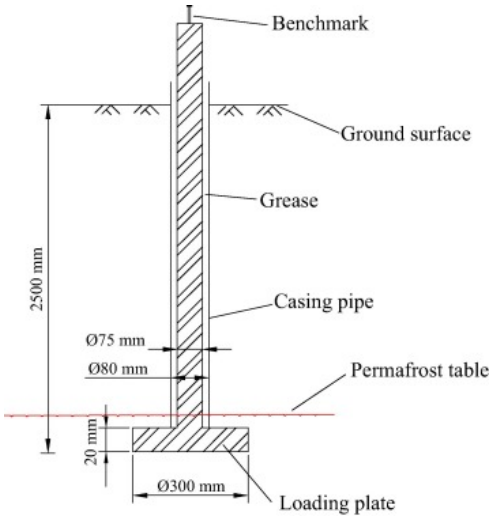

Figure 5.1 Vertical profile of the loading pile (After Zhang et al. [48])

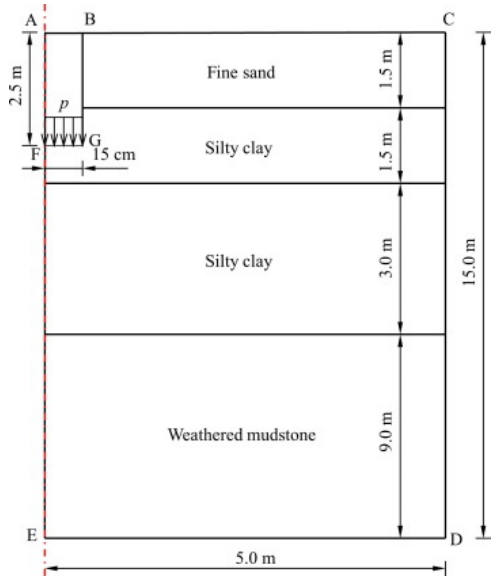

Figure 5.2 Geometry of the model (After Zhang et al. [48])

Since the reported information on the mechanical behavior of the soil is very general and limited, in the simulation, hypothetical soil parameters are used and the results are verified qualitatively. In addition, constant temperature of -1^{o}C and -2^{o}C are, respectively, considered for non-winter and winter times. Model parameters are listed in table 5.2. Since the purpose of this example is to check the ability of the model for simulating the creep deformation of a frozen soil in a permafrost region, suction induced deformation is neglected, and the related parameters, κ_s and λ_s, are assumed to be zero.

Table 5.2 Model parameters for the plate loading test

Parameter	Units	Fine Sand	Silty Clay 1	Silty Clay 2	Mudstone
Model-ID	-	15211522	15211522	15211522	15211522
Temp_Ref	K	273.16	273.16	273.16	273.16
E_{fRef}	Pa	160E6	140E6	150E6	190E6
E_{fIncr}	Pa/K	15E6	10E6	10E6	5E6
ν_f	-	0.48	0.45	0.46	0.48
G_0	Pa	4E6	5E6	8E6	15E6
κ_0	-	0.01	0.02	0.02	0.01
p^*_c	Pa	-7000	-5000	-5000	-5000
λ_0	-	0.07	0.2	0.2	0.09
γ	-	0.01	0.1	0.05	0.1
K_{t1}	-	0.25	0.35	0.25	0.45
M	-	1.1	0.85	0.95	1.25
λ_s	-	0	0	0	0
κ_s	-	0	0	0	0
r	-	0.59	0.49	0.49	0.57
β	Pa^{-1}	0.1E-6	0.15E-6	0.15E-6	0.12E-6
λ_r	-	0.5	0.5	0.5	0.5
p_r	Pa	0.1E4	0.1E4	0.1E4	0.1E4
α	-	9	9	9	9
Thawing $Temp_{Ref}$	K	273.16	273.16	273.16	273.16
Thawing $Press_{Ref}$	Pa	-395E6	-395E6	-395E6	-395E6
K_{t2}	-	2.5	1.5	1.5	1
μ_0	s^{-1}	0.01E-6	0.08E-6	0.1E-6	0.1E-9
N_0	-	35	28	28	40
b_1	Pa^{-1}	2E-6	1E-6	1E-6	0.03E-3
b_2	-	5	7	7	2
OCR	-	1.7	1.5	1.8	1.8
Initial segregation suction	Pa	15E6	15E6	15E6	15E6
Initial void ratio	-	0.3	0.25	0.25	0.2
Min. Ini. P^*_{Y0R}	Pa	-40E3	-40E3	-40E3	-40E3
P_{at}	Pa	-100E3	-100E3	-100E3	-100E3
K_w	Pa	1E9	1E9	1E9	1E9

Figure 5.3 shows the displacement contour at the end of the analysis. The time-displacement curve for a node just below the plate center is presented figure 5.4. As shown in the figure, as the load level increases, the creep rate increases. While, the creep rate decreases with decreasing temperature, e.g. during winter time of 2009-2011. This behavior is consistent with the reported settlements of this field [48], and also with the reported behavior in Eckardt [47].

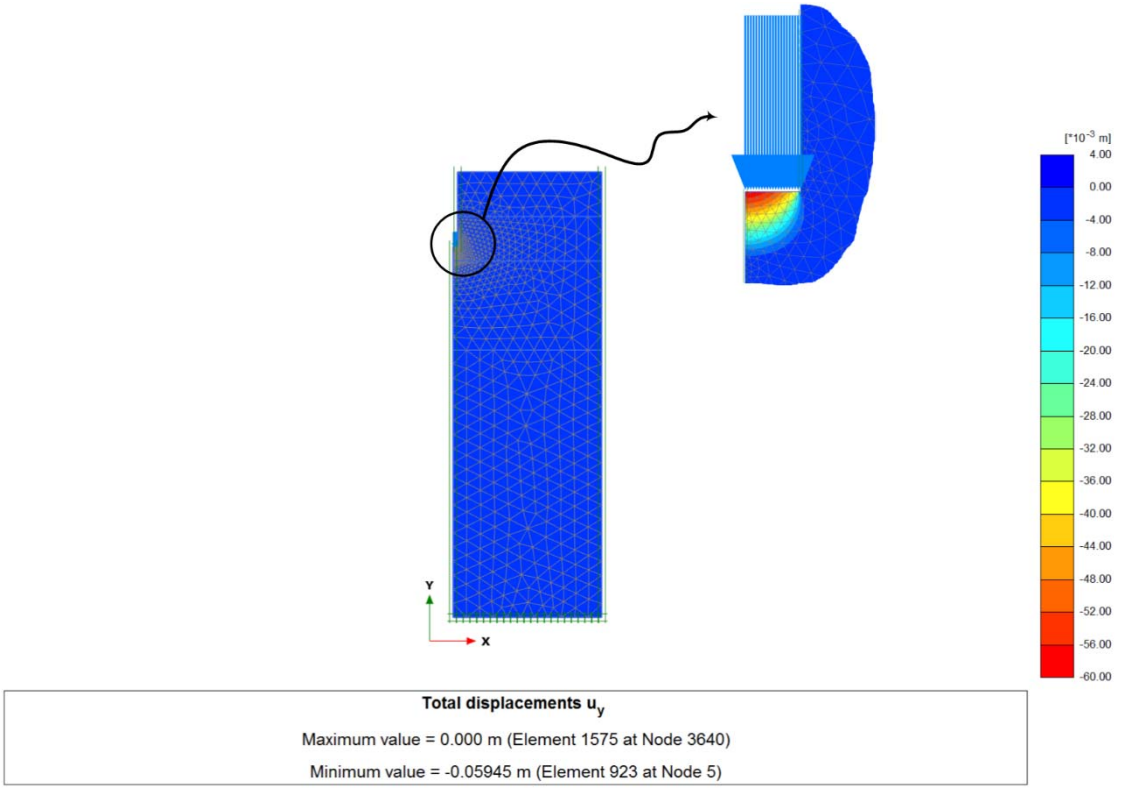

Figure 5.3 Displacement contour in September 2014

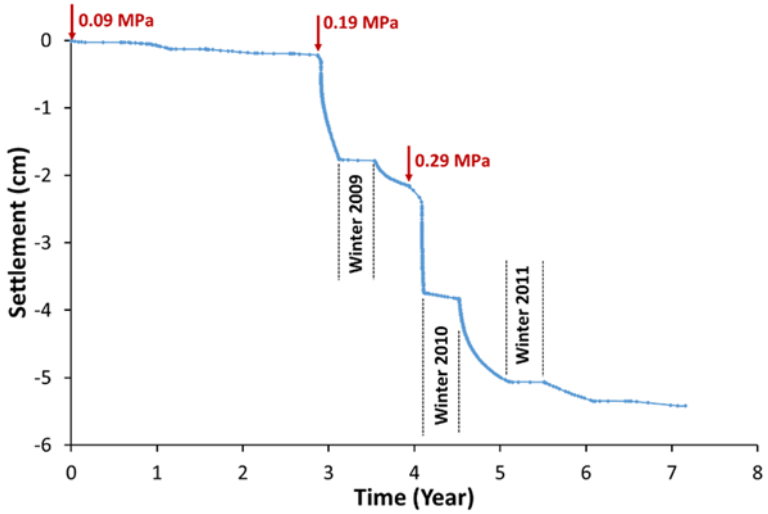

Figure 5.4 Time-settlement curve for a node below the plate center

6 References

1. Zhang, T., et al., *Further statistics on the distribution of permafrost and ground ice in the Northern Hemisphere.* Polar Geography, 2000. **24**(2): p. 126-131.
2. He, P., Y. Zhu, and G. Cheng, *Constitutive models of frozen soil.* Canadian Geotechnical Journal, 2000. **37**(4): p. 811-816.
3. Arenson, L.U. and S.M. Springman, *Mathematical descriptions for the behaviour of ice-rich frozen soils at temperatures close to 0 °C.* Canadian Geotechnical Journal, 2005. **42**(2): p. 431-442.
4. Lai, Y., et al., *Strength distributions of warm frozen clay and its stochastic damage constitutive model.* Cold Regions Science and Technology, 2008. **53**(2): p. 200-215.
5. Lai, Y., L. Jin, and X. Chang, *Yield criterion and elasto-plastic damage constitutive model for frozen sandy soil.* International Journal of Plasticity, 2009. **25**(6): p. 1177-1205.
6. Yuanming, L., et al., *Strength criterion and elastoplastic constitutive model of frozen silt in generalized plastic mechanics.* International Journal of Plasticity, 2010. **26**(10): p. 1461-1484.
7. Zhu, Z., J. Ning, and W. Ma, *A constitutive model of frozen soil with damage and numerical simulation for the coupled problem.* Science China Physics, Mechanics and Astronomy, 2010. **53**(4): p. 699-711.
8. Yang, Y., Y. Lai, and X. Chang, *Experimental and theoretical studies on the creep behavior of warm ice-rich frozen sand.* Cold Regions Science and Technology, 2010. **63**(1–2): p. 61-67.
9. Xu, G., *Hypoplastic constitutive models for frozen soil*. 2014, Ph.D Dissertation, University of Natural Resources and Life Sciences, Vienna.
10. Wang, S., et al., *A simple rheological element based creep model for frozen soils.* Cold Regions Science and Technology, 2014. **106–107**: p. 47-54.
11. Nixon, J.F., *Discrete ice lens theory for frost heave in soils.* Canadian Geotechnical Journal, 1991. **28**(6): p. 843-859.
12. Nicolsky, D.J., et al., *Modeling biogeophysical interactions in nonsorted circles in the Low Arctic.* Journal of Geophysical Research: Biogeosciences, 2008. **113**(G3): p. G03S05.
13. Li, N., et al., *Theoretical modeling framework for an unsaturated freezing soil.* Cold Regions Science and Technology, 2008. **54**(1): p. 19-35.
14. Thomas, H.R., et al., *Modelling of cryogenic processes in permafrost and seasonally frozen soils.* Géotechnique, 2009. **59**(3): p. 173-184.
15. Nishimura, S., et al., *THM-coupled finite element analysis of frozen soil: formulation and application.* Géotechnique, 2009. **59**(3): p. 159-171.
16. Zhou, M.M., *Computaional simulation of freezing: Multiphase modeling and strength upscaling*. 2014, Ph.D Dissertation, Ruhr University Bochum.
17. Zhang, Y. and R.L. Michalowski, *Thermal-Hydro-Mechanical Analysis of Frost Heave and Thaw Settlement.* Journal of Geotechnical and Geoenvironmental Engineering, 2015. **141**(7): p. 04015027.
18. Baker, T.H.W., *Strain rate effect on the compressive strength of frozen sand.* Engineering Geology, 1979. **13**(1–4): p. 223-231.
19. Ting, J., R. Torrence Martin, and C. Ladd, *Mechanisms of Strength for Frozen Sand.* Journal of Geotechnical Engineering, 1983. **109**(10): p. 1286-1302.
20. Sayles, F., *Low temperature soil mechanics*. 1966, U.S. Army, Cold Regions Research and Engineering Laboratory, Technical note.
21. Parameswaran, V.R. and S.J. Jones, *Triaxial testing of frozen sand.* Journal of Glaciology, 1981. **27**(95): p. 147-155.

22. Bragg, R.A. and O.B. Andersland, *Strain rate, temperature, and sample size effects on compression and tensile properties of frozen sand.* Engineering Geology, 1981. **18**(1–4): p. 35-46.
23. Youssef, H., *Mechanical properties and behaviour of frozen soils*, in *International Offshore and Navigation Conference and Exhibition*. 1986. p. 299-322.
24. Xie, Q., Z. Zhu, and G. Kang, *Dynamic stress–strain behavior of frozen soil: Experiments and modeling.* Cold Regions Science and Technology, 2014. **106-107**: p. 153-160.
25. Yamamoto, Y. and S.M. Springman, *Axial compression stress path tests on artificial frozen soil samples in a triaxial device at temperatures just below 0 °C.* Canadian Geotechnical Journal, 2014. **51**(10): p. 1178-1195.
26. Chamberlain, E., C. Groves, and R. Perham, *The mechanical behaviour of frozen earth materials under high pressure triaxial test conditions.* Géotechnique, 1972. **22**(3): p. 469 –483.
27. Arenson, L.U., M.M. Johansen, and S.M. Springman, *Effects of volumetric ice content and strain rate on shear strength under triaxial conditions for frozen soil samples.* Permafrost and Periglacial Processes, 2004. **15**(3): p. 261-271.
28. Sinitsyn, A. and S. Løset, *Strength of frozen saline silt under triaxial compression with high strain rate.* Soil Mechanics and Foundation Engineering, 2011. **48**(5): p. 196-202.
29. Lai, Y., et al., *An experimental investigation of the mechanical behavior and a hyperplastic constitutive model of frozen loess.* International Journal of Engineering Science, 2014. **84**: p. 29-53.
30. Henry, K.S., *A review of the thermodynamics of frost heave*. 2000: US Army Corps of Engineers.
31. Tice, A.R., D.M. Anderson, and A. Banin, *The prediction of unfrozen water contents in frozen soils from liqiud limit determinations*. 1976: US Army Corps of Engineers.
32. Koopmans, R.W.R. and R.D. Miller, *Soil Freezing and Soil Water Characteristic Curves.* Soil Science Society of America Journal, 1966. **30**(6): p. 680-685.
33. Miller, R.D. *Frost heaving in non-colloidal soils*. in *3rd Int. Conf. on Permafrost*. 1978. Edmonton.
34. Black, P.B. and A.R. Tice, *Comparison of soil freezing curve and soil water curve data for Windsor sandy loam.* Water Resources Research, 1989. **25**(10): p. 2205-2210.
35. Grant, S. and R. Sletten, *Calculating capillary pressures in frozen and ice-free soils below the melting temperature.* Environmental Geology, 2002. **42**(2-3): p. 130-136.
36. Coussy, O., *Poromechanics of freezing materials.* Journal of the Mechanics and Physics of Solids, 2005. **53**(8): p. 1689-1718.
37. Wettlaufer, J.S. and M.G. Worster, *Premelting dynamics.* Annual Review of Fluid Mechanics, 2006. **38**(1): p. 427-452.
38. Rempel, A.W., J.S. Wettlaufer, and M.G. Worster, *Premelting dynamics in a continuum model of frost heave.* Journal of Fluid Mechanics, 2004. **498**: p. 227-244.
39. Vlahou, I., *Freeze fracturing of elastic porous media*. 2012, Ph.D Dissertation, University of Cambridge.
40. Suklje, L. *The analysis of the consolidation process by the isotaches method*. in *the proceeding of 4th Int. Conf. on Soil Mechanics and Foundation Engineering (ICSMFE)*. 1957. Butterworths Scientific, London.
41. Bjerrum, L., *Engineering Geology of Norwegian Normally-Consolidated Marine Clays as Related to Settlements of Buildings.* Géotechnique, 1967. **17**(2): p. 83-118.
42. Janbu, N. *The resistance concept applied to deformation of soils*. in *Proc. 7th Int. Conference on SMFE*. 1969. Mexico city.

43. Grimstad, G. and S.A. Degago, *A non-associated creep model for structured anisotropic clay (n-SAC)*, in *Numerical Methods in Geotechnical Engineering*. 2010, CRC Press. p. 3-8.
44. Alonso, E.E., A. Gens, and A. Josa, *A constitutive model for partially saturated soils.* Géotechnique, 1990. **40**(3): p. 405-430.
45. Perzyna, P., *Fundamental Problems in Viscoplasticity*, in *Advances in Applied Mechanics*, H.L.D.P.G.L.H.W.O.W.P.R.F.P. G.G. Chernyi and H. Ziegler, Editors. 1966, Elsevier. p. 243-377.
46. Zhu, Y. and D.L. Carbee, *Uniaxial compressive strength of frozen silt under constant deformation rates.* Cold Regions Science and Technology, 1984. **9**(1): p. 3-15.
47. Eckardt, H., *Creep behaviour of frozen soils in uniaxial compression tests.* Engineering Geology, 1979. **13**(1): p. 185-195.
48. Zhang, H., et al., *A consolidation model for estimating the settlement of warm permafrost.* Computers and Geotechnics, 2016. **76**: p. 43-50.

Document information		
Document title Enhanced permafrost model – documentation & user manual		**Document no:** PIAG_GA_2011-286397-R6
Document type X **Report** □ **Technical note**	**Distribution** X **Public** □ **Limited** □ **None**	**Date:** 2016-01-31 **Rev.no.** 0
Client EU CREEP project		
Keywords creep, permafrost		

Place:
Country, province Norway
Municipality Trondheim
Location NTNU
Map sheet -
UTM coordinates -

Document control

Quality control after own QC system

Rev.	Rev. on basis of	Self-check:		Internal control		Independent control:	
0	Original document	SAGA		GG			

Document approved for publishing	**Date**	**Sign. PM.**
GG	2016-01-31	GG